Chemistry Theses   Chemistry

11-2019

Alginate/Cucurbit [7] Uril/Dequalinium–Basedb Supramolecular Carbohydrates: Modulation of Fret Signal by Temperature Control

Amir Sohail Noor Alam Jan

United Arab Emirates University

College of Science

Department of Chemistry

ALGINATE/CUCURBIT[7]URIL/DEQUALINIUM–BASED
SUPRAMOLECULAR CARBOHYDRATES: MODULATION OF
FRET SIGNAL BY TEMPERATURE CONTROL

Amir Sohail Noor Alam Jan

This thesis is submitted in partial fulfillment of the requirements for the degree of
Master of Science in Chemistry

Under the Supervision of Dr. Na'il Saleh

November 2019

Declaration of Original Work

I, Amir Sohail Noor Alam Jan, the undersigned, a graduate student at the United Arab Emirates University (UAEU), and the author of this thesis entitled *"Alginate/Cucurbit[7]uril/Dequalinium-Based Supramolecular Carbohydrates: Modulation of FRET Signals by Temperature Control"*, hereby, solemnly declare that this thesis is my own original research work that has been done and prepared by me under the supervision of Dr. Na'il Saleh in the College of Science at UAEU. This work has not previously been presented or published, or formed the basis for the award of any academic degree, diploma or a similar title at this or any other university. Any materials borrowed from other sources (whether published or unpublished) and relied upon or included in my thesis have been properly cited and acknowledged in accordance with appropriate academic conventions. I further declare that there is no potential conflict of interest with respect to the research, data collection, authorship, presentation and/or publication of this thesis.

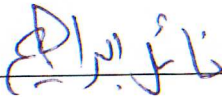Student's Signature: _____ Date: 6/1/2020
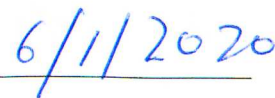
Approval of the Master Thesis

This Master Thesis is approved by the following Examining Committee Members:

1) Advisor (Committee Chair): Na'il Saleh Ibrahim

   Title: Associate Professor

   Department of Chemistry

   College of Science

   Signature _____   Date ___Dec. 8th, 2019___

2) Member: Mohamed Alazab Alnaqbi

   Title: Associate Professor

   Department of Chemistry

   College of Science

   Signature _____   Date ___11/12/2019___

3) Member (External Examiner): Pance Naumov

   Title: Associate Professor
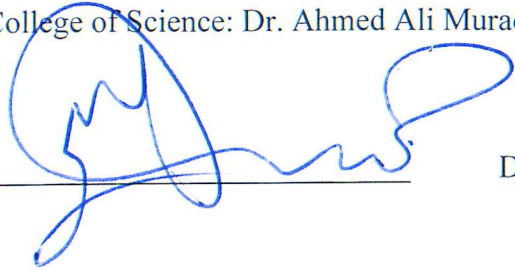
   Department of Chemistry

   Institution: New York University, Abu Dhabi, UAE

   Signature _____   Date ___10/10/2019___

This Master Thesis is accepted by:

Dean of the College of Science: Dr. Ahmed Ali Murad.

Signature _____   Date _7/11/2020_

Dean of the College of Graduate Studies: Professor Ali Al-Marzouqi

Signature _Ali Hassan_   Date _8/1/2020_

Copy _5_ of _5_

Abstract

Herein, we describe the synthesis of a bioactive, inexpensive, and easy-to-handle supramolecular carbohydrate polymer by grafting of cucurbit[7]uril macrocycle (CB7)-encapsulated dequalinium chloride hydrate (DCH) onto alginic acid carbohydrates (ALG) via amide linkage formation and show that light energy transfer based on energy migration can be controlled by altering polymer temperature without changing polymer composition. DCH (donor) and 2-anilinonaphthalene-6-sulfonic acid (acceptor) were used to generate Förster resonance energy transfer (FRET) signals. Stationary and time-resolved photoluminescence spectra of the modified carbohydrate platform revealed that FRET resulted in a color change from violet (~387 nm) to blue (~429 nm), which could be repeatedly switched on and off in response to temperature stimuli at 298–368 K. NMR measurements suggested that the responsiveness of DCH/CB7ALG to thermal stimuli was due to the threading of CB7 onto the DCH backbone in solution and upon grafting onto ALG polymers.

Keywords: Energy Transfer, Cucurbiturils, Alginates, Dequalinium, Molecular Shuttling, Stimuli-Responsiveness, Temperature Control, Luminescence, Time-Resolved Photoluminescence.

Title and Abstract (in Arabic)

الكربوهيدرات من جزيئات حمض الجينيك-الكوكوربيتيوريل السابع- ديكوالينيوم: عملية انتقال إشارات فروستر من خلال التحكم في درجة الحرارة

الملخص

يصف هذا العمل تركيب بوليمركربوهيدرات نشط, حيوي، و غير مكلف و سهل التعامل معه. و ذلك بربط جزيئات هيدرات كلوريد ديكوالينيوم المغلفة بمركبات الكوكوربتيوريل السابعة برابطة أميدية على حمض الجينيك. أظهر هذا الإرتباط إمكانية التحكم في انتقال الطاقة عن طريق تغيير درجة حرارة البوليمر دون الحاجة لتغيير تركيبه. تم استخدام مركب دكيوالينيوم (المانح) و حمض 2-أنيلونونافثالين-6 (المستقبل) سويا لتوليد الإشارات الرنينية لطاقة فروستر. أظهرت نتائج التوهج الضوئي والقياسات الزمنية لهذه الكربوهيدرات المعدلة انتقال الطاقة مما أدى إلى تغيير اللون من اللون البنفسجي (387 نانومتر) إلى اللون الأزرق (حوالي 429 نانومتر), و الذي يمكن تشغيله و ايقافه بشكل متكرر استجابة لمنبهات درجة الحرارة عند 298-368 كالفن. كما أظهرت نتائج القياسات الطيفية للرنين المغناطيسي أن عملية الإستجابة الحرارية تحدث عن طريق انتقال جزيئات الكوكوربتيوريل أثناء دورانها حول سلاسل البوليمر.

مفاهيم البحث الرئيسية: انتقال الطاقة، الكوكوربتيوريل، حمض الجينيك، ديكوالينيوم، محفزات استجابية، التحكم في درجة الحرارة، التوهج الضوئي، القياسات الزمنية للتوهج الضوئي.

Acknowledgements

I sincerely thank and appreciate my supervisor Dr. Na'il Saleh for giving me the opportunity to work in his research projects, which further amplify my knowledge and research skills in the science of photochemistry. I am grateful to his constant help and guidance in the light of his precious knowledge and experience.

I would like to thank the chairman, Dr. Mohamed Alazab and all members of the Department of Chemistry at the United Arab Emirates University, for their continuous support as a master student.

My notable acknowledgment goes to my parents, brothers, and sisters for their unconditional encouragement and support in all stages of my life.

Dedication

To my beloved parents and family

Table of Contents

List of Tables

List of Figures

List of Abbreviations

ALG	Alginic Acid
ANS	2-Anilino-Naphthalene-6-Sulfomic Acid
CB7	Cucurbit[7]uril
DCH	Dequalinium Chloride Hydrates
DCC	N,N'-Dicyclohexylcarbodiimide
DMAP	4-Dimethylaminopyridine
DLS	Dynamic Light Scattering
FRET	Förster Resonance Energy Transfer
FTIR	Fourier Transform Infrared Spectroscopy
IRF	Instrument Response Function
NMR	Nuclear Magnetic Resonance
PL	Photoluminescence
SEM	Scanning Electron Microscopy
TRPL	Time-Resolved Photoluminescence

Chapter 1: Introduction

1.1 Overview

Supramolecular nanostructured materials, which display Förster resonance energy transfers (FRET) signals, have become the focus of interest for many researchers across the globe. Supramolecular light harvesting system is based on light energy transfer from one molecule to another following different mechanism of light energy transfer. FRET based systems were used in various applications such as cancer diagnosis[1], artificial photosynthesis[2], security encryption,[3] and fluorescent ink.[4]

1.2 Statement of the problem

To link carbohydrate platform to dequalinium chloride hydrates (DCH) through an amide linkage with and without cucurbit[7]uril (CB7) as shown in below (Figure 1).
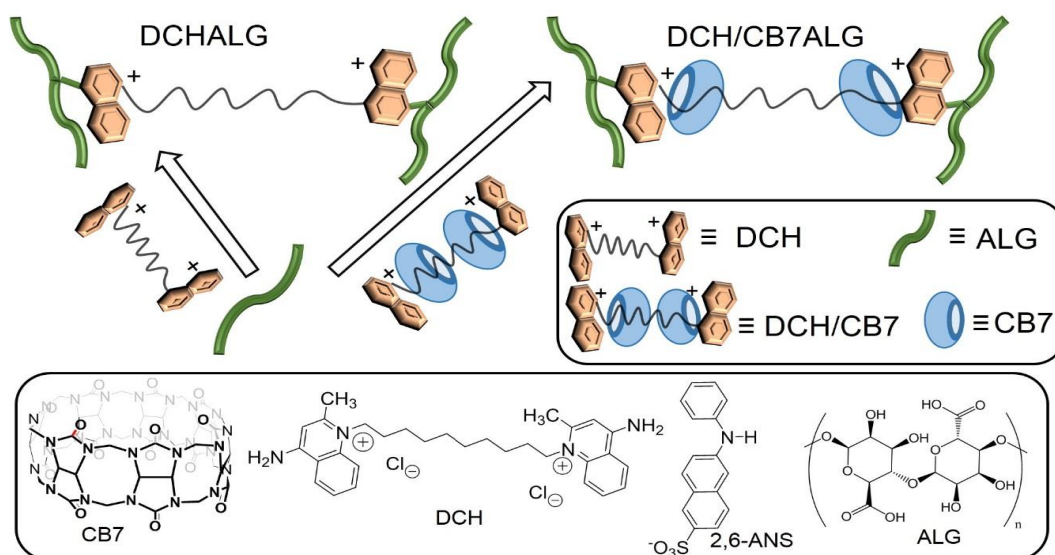
Figure 1: Chemical structures of the donor DCH, acceptor ANS along with CB7 macrocycles and ALG carbohydrate. A cartoonic view for the covalent conjugation to ALG with and without CB7 is also illustrated.

To verify that the FRET signal in the modified carbohydrate polymer can be reversibly controlled in response to temperature stimuli Moreover, the aim is to explore how temperature sensing is related to CB7 shuttling along DCH axle.

1.3 Host-guest chemistry

Our newly constructed supramolecular polymer is based on utilizing the molecular recognition and assemblies of CB7 towards DCH. Supramolecular science governs the non-covalent interactions for bringing two or more molecules together (Figure 2). One molecule (the host) sequester another one (the guest) utilizing the non-covalent interactions, which include hydrogen bonding, metal coordination, hydrophobic forces, van der Waals forces, π-π interactions and electrostatic interactions. The operating of these non-covalent forces in supramolecular chemistry widen its applications in different fields of research.

Guest molecules may be cationic/neutral species or derivatives of carboxylic acid/ammonium whereas the host molecule is a pocket-like cavity, such as cucurbit[n]uril, cyclodextrin and pillar[n]arene. The encapsulation of guest molecules by the host results in the formation of a host-guest complex by analogy to the formation of a substrate-enzyme complex. When guest molecules bind to host molecules, significant changes are expected in their physical, chemical and biochemical properties. The host-guest chemistry also rationalizes the establishment of three-dimensional structure of large supramolecular architecture.
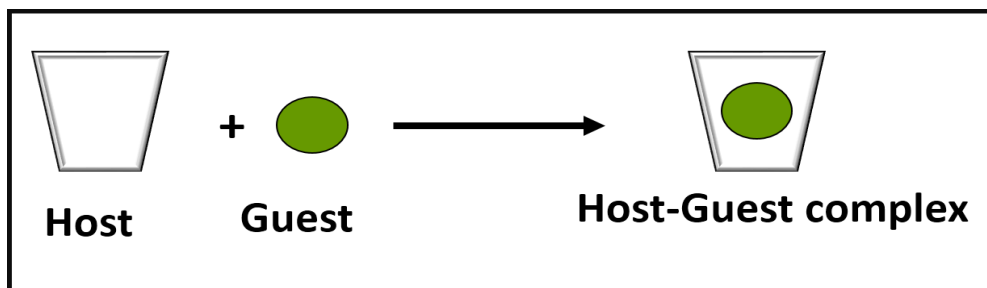
Figure 2: The host and guest linked via non-covalent interactions forming a host-guest complex.

From a thermodynamics perspective, the guest is stabilized in the large cavity of the host by weak physical interactions in accordance with equation (1).

$$H + G \rightleftharpoons HG \qquad (1)$$

Equilibrium constant K_a is given by equation (2).

$$K_a = \frac{[HG]}{[H][G]} \qquad (2)$$

Large K_a value represents strong interaction of host guest complex.

Gibbs free energy (ΔG^0) of host guest complex is determined by equation (3).

$$\Delta G^o = -RT \ln K_a \qquad (3)$$

R stands for gas constant, T is temperature, K_a is used for denoting equilibrium constant and ln stands for natural logarithm.

The entropy changes for host-guest complex (ΔS_{exp}) are associated with configuration entropy ($\Delta S_{conf.}$) and changes attributed to solvation entropy (ΔS_{solv}). This can be summarized by Eq. 4.

$$\Delta S_{exp} = \Delta S_{conf} + \Delta S_{solv} \tag{4}$$

The benefit from employing the supramolecular approach is to facilitate FRET in light harvesting system. The harnessing of light energy by the host molecules in FRET materials also expand their use in other applications in which reversibility and stimuli responsiveness play a major role.

1.4 Photoluminescence phenomena

The glowing of molecules upon absorbing a specific light energy is termed as photoluminescence. Based on the type of relaxation from higher to lower electronic state, photoluminescence is divided into two sub-headings: fluorescence and phosphorescence (Figure 3). The relaxation of excited electron with the same spin is termed as fluorescence and it occurs within 10^{-9} s while change in the spin of excited electron relative to its spin in the ground state leads to phosphorescence. The change in the spin of excited electron affects the rates of emission and decays of the excited molecule.

The interaction of light with molecules leads to excitation from ground state to higher energy electronic state (S_1 or S_2) and this transition occurs in a time scale of 10^{-15} s. The excited electron (S_1 or S_2), upon relaxation loses the absorbed energy either radiatively or non-radiatively. Radiative transition is based on the absorption of photon to high energy level or loss of energy (emission) from high energy to lower energy level. Non-radiative transitions follows different pathways of relaxation. In the excited state (S_1 or S_2), the non-radiative relaxation occur from high vibrational level to low vibrational level (vibrational relaxation) causing the loss of energy as heat to the surrounding media within 10^{-12} s. The second non-radiative transitions is the internal

conversion based on relaxation from high excited state (S_2), to low excited state (S_1) level. Intersystem crossing (ISC) is the third type of transition to a state of spin with different multiplicity (T) in which electronic transition occurs from S_1 to first electronic state T_1. The transition to state of different spin multiplicity (T) generates phosphorescence with an average lifetime from 10^{-5} to $>10^{+3}$ sec. The excited electron relaxing from triplet to singlet ground state have longer lifetime as compared to the electron relaxing from singlet excite state to singlet ground state. As a summary, fluorescence arises from the lowest energy level (S_1) in a time scale of nanoseconds while phosphorescence starts from T_1 to the ground sate with a much longer time than fluorescence.[5] All the radiative and non-radiative relaxation pathways are shown in the Jablonski diagram (Figure 3).
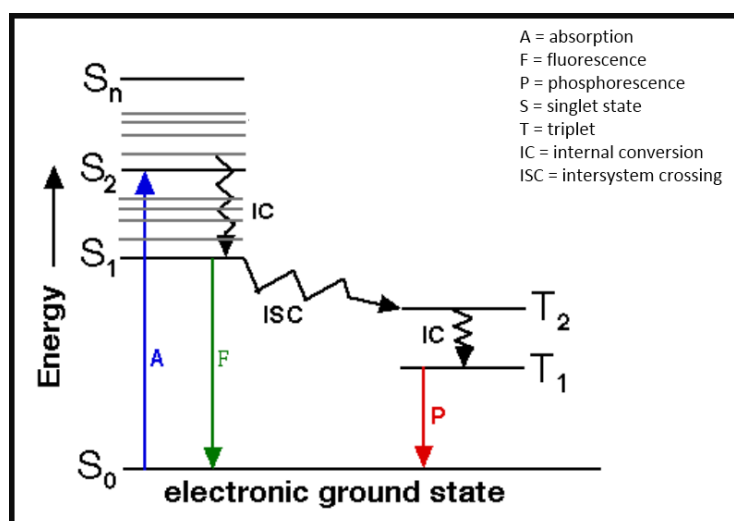
Figure 3: Fluorescence and phosphorescence with radiative and radiative transition from excited electronic state to the ground state.

Photochemically, when a molecule is excited to high electronic state, the time that an excited molecule spends in high energy levels is called an *excited-state lifetime* and it explains the behaviour of fluorescent molecule in the excited state. The factors

affecting the excited-state lifetime value, includes the structure of molecule and the surrounding local environment. In addition to excited-state lifetime, *fluorescence quantum yield* is normally used to characterize the emission of a fluorophore. The ratio of the intensity of the emitted light intensity to that of the absorbed light is termed as Quantum yield (ϕ).

$$\phi = \frac{Intesity\ of\ emitted\ fluorescence}{Intensity\ of\ absorbed\ light} = \frac{I_f}{I_{abs}} \tag{5}$$

Consider the below kinetic mechanism for the transfer of molecules from the ground state to the excited state:

$$\text{Absorption: } M + light \rightarrow M^* \qquad rate = I_{abs}$$

$$\text{Radiative decay: } M^* \rightarrow M + light \qquad rate = k_r[M^*]$$

$$\text{Non-radiative decay: } M^* \rightarrow M \qquad rate = k_{nr}[M^*]$$
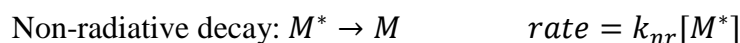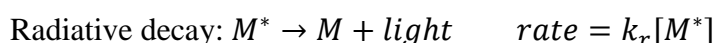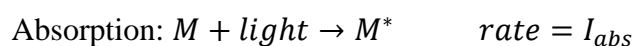
Applying the steady-state approximation, the excited species, M* gives the following kinetic expression:

$$\frac{d[M^*]}{dt} = I_{abs} - k_r[M^*] - k_{nr}[M^*] = I_{abs} - (k_r + k_{nr})[M^*] = 0$$

$$I_{abs} = (k_r + k_{nr})[M^*]$$

Substituting in eq (5) leads to the following expression for quantum yield (eq 6):

$$\phi = \frac{k_r}{k_r + k_{nr}} \tag{6}$$

By observing only the decay pathways of the excited fluorophore in Eqs. 2 and 3, the change in concentration of excited species (M*) with time becomes:

$$\frac{-d[M^*]}{dt} = k_r[M^*] + k_{nr}[M^*]$$

By integrating, the final rate law is obtained as:

$$[M^*] = [M]_0 \, e^{-(k_r+k_{nr})t}$$

Excited-state lifetime τ is the time at which the concentration of excited molecule at the first singlet state reaches 0.368 ($1/e$) of its initial value and after excitation is usually referred to as (τ), and it is equal to the reciprocal of decay rate constant ($K_r + K_{nr}$):

$$\tau = \frac{1}{k_r + k_{nr}} \tag{7}$$

Excited-state lifetime *(τ)* can also be expressed as:

$$\tau = \frac{1}{k_r + k_{nr}} = \frac{\phi}{k_r} \tag{8}$$

1.5 Steady-state and time-resolved photoluminescence measurement

Fluorescence measurement is one of the spectroscopic tool for understanding the type of reactions in the excited state of the molecule. The photoluminescence decay with time gives more accurate information about the behaviour of the excited species. Both techniques are used for measuring samples in solution or in solid state utilizing specific sample holder.

Experimentally, while collecting photoluminescence (PL) data, the sample is exposed to flash of light (laser) and the emitted signal is recorded continuously as a function of the emitted wavelength. The PL technique is very sensitive method to the extent that it detects conformational changes in the sample. For a quantitative measurement, the emission of photons (fluorescence) is also studied by Time-

Resolved Photoluminescence (TRPL) techniques. Lifetime obtained by utilizing TRPL technique, is affected by the nature of solvent, quencher, levels of O_2 and temperature. The other factors affecting decay kinetics include inter and intramolecular process in the excited state. Studying the kinetics in the excited state also unfold the reaction mechanism.

When a suitable light pulse excites the fluorophore, a very fast detector is used to quantify the emission of the fluorophore as a function of time. The decay of its emission intensity (I(t)) is represented by an exponential decay equation, as follows:

$$I(t) = I_0\, e^{-t/\tau} \tag{9}$$

Where I_0 is the intensity at time = 0 and τ is the excited state lifetime.
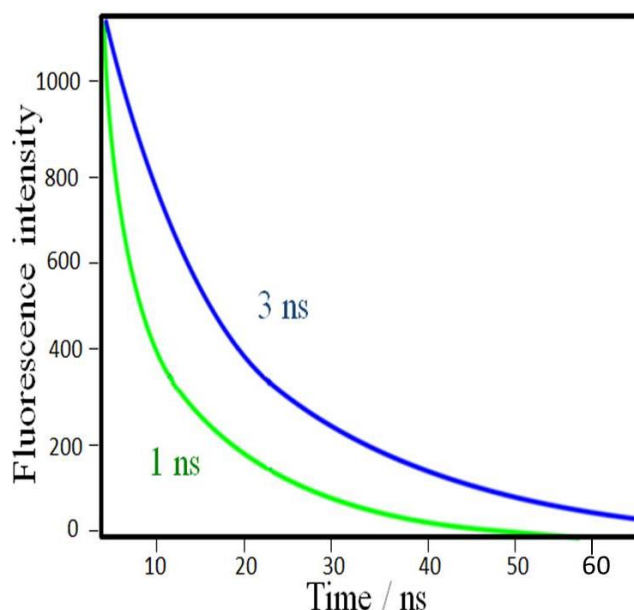
Figure 4: Emission decay with two species of a fluorophore, which are characterized by different excited state lifetime.

TRPL is helpful in sorting out fluorophores with different single exponential decay and lifetime as shown in Figure 4. For the mixture of fluorophore the sum of exponentials decay functions is given by:

$$I(t) = \sum_{i=0}^{n} \alpha_i \, e^{-t/\tau_i} \tag{10}$$

where α represents the contribution of each fluorophore i to the total decay function and τ_i is the individual excited-state lifetime. However, the fraction that each decay contributes to the PL spectrum is calculated by f_i:

$$f_i = \frac{\alpha_i \tau_i}{\sum_j \alpha_j \tau_j} \tag{11}$$

Experimentally, the instrument response function (IRF), appeared in the measured emission decay reflecting the time resolution of the instrument. A specialized sample called Ludox is used for collecting instrument response function (IRF) relative to the emission decay[6] as shown in Figure 5.
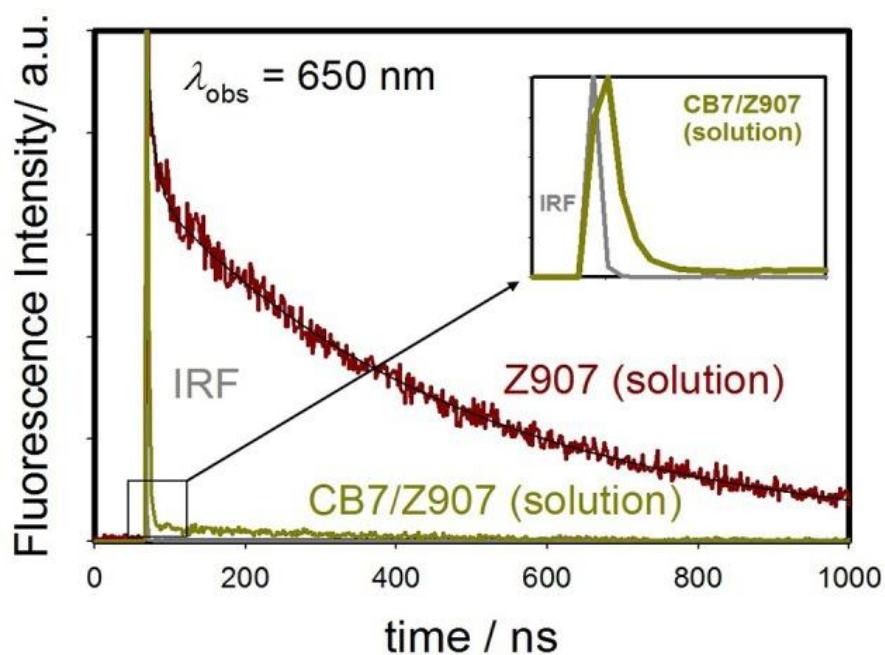
Figure 5: Emission decay of a fluorophore monitored at 650 nm in acetonitrile and water. The inset expands the region in 10ns range to unfold the IRF decay profile.

1.6 Kinetics of intermolecular process

Fluorescence quenching is defined as, the decline in the fluorescence intensity of fluorescent species, through various intermolecular interactions such as proton transfer, energy transfer, electron transfer and ground state complex formation. The gradual decrease in the emission of donor with concomitant increase of the acceptor emission is an indication for the occurrence of energy transfer.

(a) Stern-Volmer kinetics

Fluorescence quenching is kinetically analysed assuming the Stern-volmer equation.

The presence of a quencher (Q) leads to a new deactivation process resulting in decreasing the emission intensity of M* (the fluorophore)

$$Q + M^* \rightarrow M + Q \qquad\qquad rate = k_q[Q]\,[M^*]$$

The observed quenched excited state lifetime τ_q and unquenched excited state τ_o becomes,

$$\tau_q = \frac{1}{k_r + k_{nr} + k_q[Q]} \qquad\qquad (12)$$

$$\tau_o = \frac{1}{k_r + k_{nr}} \qquad\qquad (13)$$

The ratio of τ_q/τ, from equations (12) and (13) becomes

$$\frac{\tau_0}{\tau} = 1 + \tau_0 k_q[Q] \qquad\qquad (14)$$

Where τ is the emission excited state lifetime in the absence of a quencher and τ_q is the emission-excited lifetime in the presence of quencher and the relation is known as the *Stern-Volmer* equation.

(b) Diffusion-controlled kinetics

When the reactant M^{*} and Q are at closest proximate and the probability of reaction is one equivalent, the reaction does not need activation energy and all collision lead to product formation. The rate constant for the reaction can then be written using Smoluchowski equation.

$$K_d = 4\pi N R_q D \tag{15}$$

where R_q is the distance of closest approach between M^{*} and Q *and* the N stands for Avogadro`s number. D is the mutual diffusion coefficient constant, which gives information about the two sphere coming into contact with one another. By using stokes Einstein relation, the diffusion constant (eq 16) can be written as:

$$D = D_A + D_B = \frac{K_B\,T}{6\pi\eta R_H} \tag{16}$$

D Translational diffusion coefficient [m²/s] – "speed of the particles"
K_B Boltzmann constant [m²kg/Ks²]
T Temperature [K]
η Viscosity [Pa.s] of media
R_H Hydrodynamic radius [m]

1.7 Förster resonance energy transfer (FRET)

The phenomena of energy transfer can be understood as processes by which the excitation energy of an excited molecule D*, the energy of donor, is absorbed by the proximate molecule A, the energy of acceptor. During energy transfer process, one fluorophore acting as donor, is excited after which transfer its energy is transferred to another fluorophore called acceptor.

$$D* + A \rightarrow D + A*$$
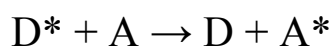
Normally, when photon energy is absorbed by the donor molecules, the excited molecules first vibrationaly relax k_{nr} from high vibration level to low vibrational level. For energy transfer to happen certain conditions must be satisfied such as excitation of donor at an appropriate wavelength, the proper orientation of both the fluorophores (donor and acceptor), the suitable distance between the two fluorophore and the spectral overlap of donor emission with acceptor absorbance.

Energy transfer takes place by two mechanisms: Dexter or Förster

1. Dexter Energy Transfers: Electron exchange interactions and orbital overlap are the prime conditions for Dexter energy transfer mechanism. Moreover, energy transfer from donor to acceptor takes place through non-radiative channel.

2. Förster Resonance Energy Transfers (FRET): Arise from the interaction of an oscillating dipolar electric field of D* and A in the space (*columbic* resonance mechanism) and the energy transfer takes place by non-radiative mode. FRET occur over large distance compared to Dexter energy transfer mechanism.

It is important to notice that acceptor A does not absorb directly the energy of incident light. The donor molecule absorbs incident light and yet emission of acceptor is observed.

The study of FRET between donor and acceptor operating in supramolecular light harvesting system utilizing TRPL measurements can be beneficial for understanding the mechanism of responsiveness to certain stimuli in newly designed functional materials.
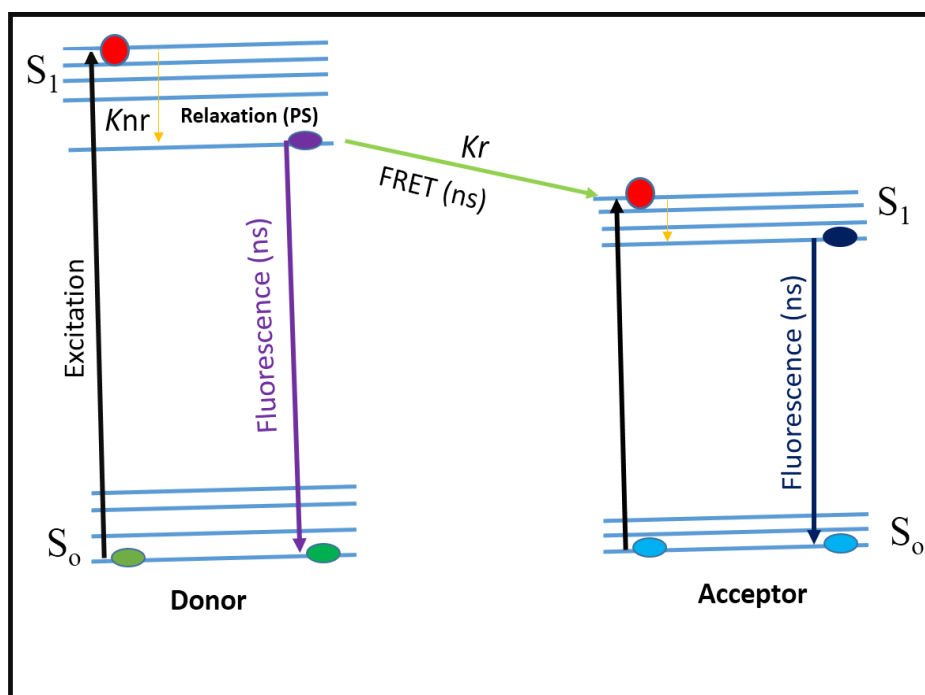
Figure 6: Electronic states of common fluorophores

Researchers for the full analysis of newly synthesized materials have used many characterization techniques. Based on each technique' principal of working, distinct characterization is helpful in understanding the structure and properties of the materials. Some of the characterization techniques are discussed below.

1.8 Dynamic light scattering (DLS)

Dynamic light scattering (DLS) is a technique that is widely used to determine the size distribution profile of small particles in suspension or polymers in solution. Dynamic light scattering (DLS) is based on the Brownian motion of dispersed particles in the solution. The dispersed particle in a liquid move randomly in all directions and the particles are constantly colliding with the solvent. This collision energy induces particle movement. The collision energy transfer has more effect on small size particle as compared to large size particle and as a result smaller particle move very fast. The viscosity and temperature of the media also affect the speed of the particles. Measuring

the particle's speed is useful in determining the hydrodynamic diameter of the particles.[7]

The relation between the speed of the particles and the particle size is given by the Stokes-Einstein equation. (Eq. 16).

The basic setup of a DLS instrument as shown in Figure 7. A single frequency laser is directed to the sample. The incident laser light upon collision with the particle gets scattered in all directions. The scattered light is detected at a certain angle over time and this signal is used to determine the diffusion coefficient and the particle size by using Stokes-Einstein equation (Eq. 16).
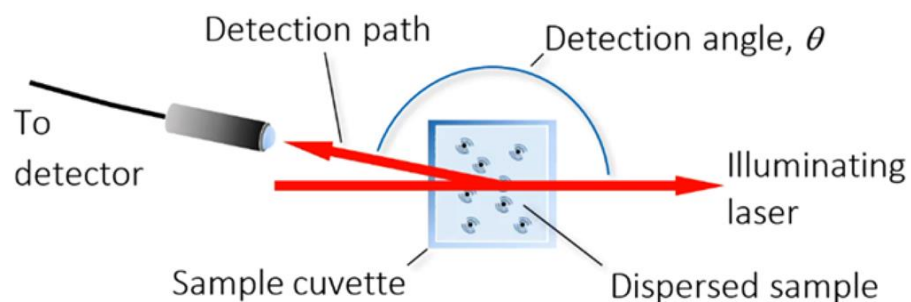
Figure 7: Schematic of a typical DLS instrument, configured to detect backscattered light from the dispersed sample.

1.9 Zeta potential

Zeta potential is one of the important techniques used in materials science for characterization of material's surface or stability of the particles in the dispersed media. When a solid comes in contact with a liquid, the functional group of the solute will interact with the surrounding media and as a result, charge is generated on the surface of the materials. The material's surface causes the accumulation of oppositely charged

ions and these counter ions arrange themselves in a fashion called electrochemical double layer. The zeta potential is the sum of the initial surface charge and the accumulated layer. Zeta potential is also established by the adsorption of ions from the solution. It must be notice that properties of the liquid medium such as pH value or buffer concentration play a key role in the generation of zeta potential. The charge formation by adsorption strongly depends on the pH value.

The charge generated on the surface of the particle leads to surface potential Ψ_0 and has an effect on the arrangement of anions and cations of the aqueous medium. The charge behavior at the solid-liquid interface is well explained using the model of the electrochemical double layer (EDL). This electrochemical double layer is comprised of two layers (stationary and diffuse layer)[8] as shown in Figure 8.

- A stationary layer is formed directly at the surface. Ions in this layer are immobilized due to strong interactions with the surface.
- The outer layer is called the diffuse layer because ions are less attracted to the surface and have the ability to move within this layer.
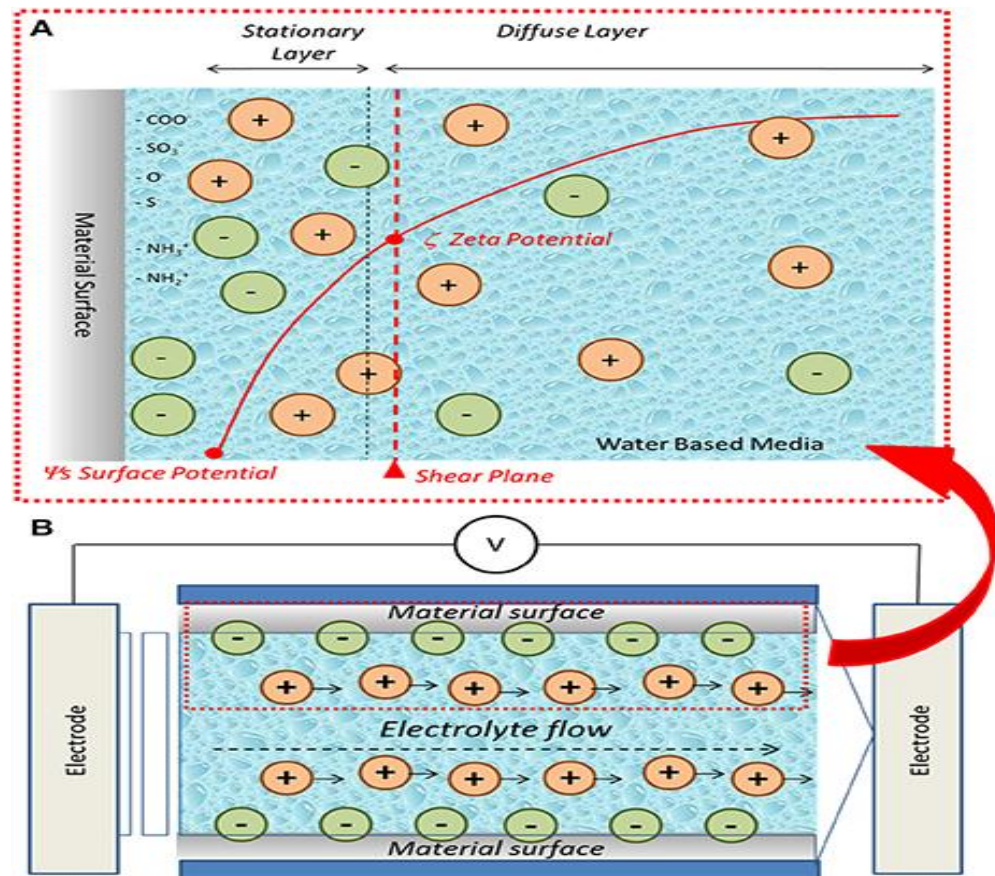
Figure 8: Schematic representation of charge development at biomaterials-water based medium interface and zeta potential.

1.10 Scanning electron microscopy (SEM)

Scanning electron microscope is the most advanced method for imaging the microstructure and morphology of the materials. The surface of the sample is focused by beam of electron. The focused beam of electron interacts with the atoms in the sample, producing different intensity signals that contain useful information about the morphology and composition of the sample. The beam of the electron scan sample side-to-side pattern and the position of the targeted beam reinforce the intensity of the detected signal, thus producing an image of the sample. In general the secondary

electrons emitted by the atom excited by the electron gun of the SEM, are detected by using secondary electron detector as shown in Figure 9.

The secondary electron is ejected from the valence or conduction band of the sample surface using electron beam as an ejection source. In secondary electron imaging (SEI), the secondary electrons are emitted from region near the material surface. SEI can produce very high-resolution images of a sample surface, magnifying details less than 1 nm in size.[9] The essential components of all SEMs include the following.

(1) Electron Source ("Gun")   (2) Electron Lenses

(3) Sample stage   (4) Detectors for all signals of interest

(5) Display / Data output device   (6) Power supply

(7) Vacuum system   (8) Cooling system
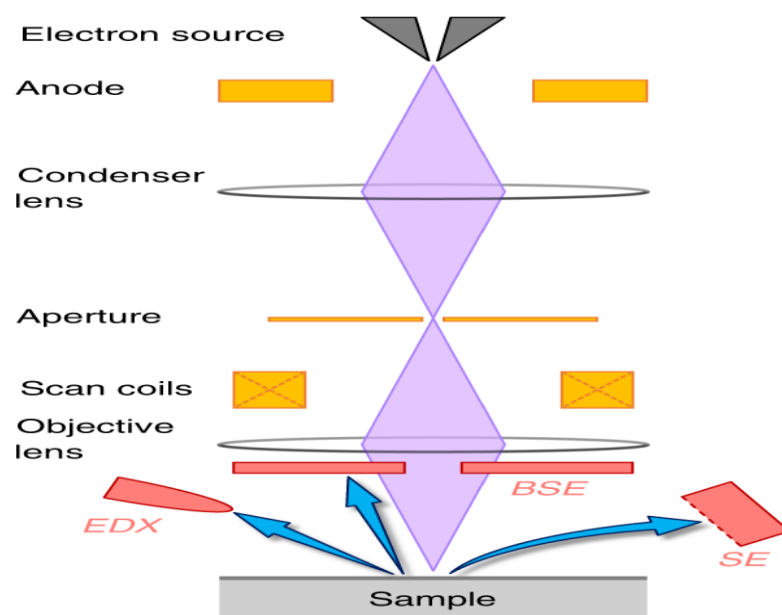
Figure 9: Schematic representation of the basic SEM components.

1.11 Literature reported supramolecular architecture

The nature-inspired tuning of light energy transfer between donor and acceptor components in artificial light-harvesting systems (based on various scaffolds such as supramolecular assemblies) has long been employed by numerous scientists in their quest for multiple fluorescence emissions.[10–13] In contrast to classical approaches, which are based on covalent conjugation, self-assembly has a higher potential to produce tunable photoluminescent materials.[13–15] In particular, supramolecular photoluminescent materials with tunable spectra continue to attract the attention of researchers working in different fields of research.

Herein, we prepare tunable photoluminescent materials on the basis of energy migration, employing alginic acid (ALG)[16] as the carbohydrate platform, dequalinium chloride hydrate (DCH) as the donor,[17] 2-anilinonaphthalene-6-sulfonic acid (2,6-ANS)[18] as the acceptor, and cucurbit[7]uril (CB7)[19,20] as the macrocycle

The above configuration was inspired by the fact that the ultrahigh affinity of CB7 to cationic guests[15,21–24] enables the sliding motion of CB7 along the guest axle,[25–28] as exemplified by CB7 threading onto a polyrotaxane backbone.[29] Consequently, the shuttling property of the CB7 host-guest system and the covalent grafting of DCH as a cationic guest onto ALG by an amide linkage were expected to generate temperature stimuli–responsive tunable emission because the grafting of CNB7 threaded DCH onto ALG sustain longer shuttling of CB7 on the DCH axle and results the whole system responsive to thermal stimuli. Additionally, all employed materials, including ALG[16] and DCH,[17] have important biomedical applications, e.g., CB7 has long been employed in diverse biological systems as a synthetic receptor[30,31] with no indication of adverse effects.[32]

Chapter 2: Experimental

2.1 Chemicals

CB7, ALG, DCH, 2,6-ANS, N,N'-dicyclohexylcarbodiimide (DCC), 4-dimethylaminopyridine (DMAP), D_2O, and DMSO-d_6 were purchased from Sigma-Aldrich (St. Louise, MO, USA) and used as received. All chemicals had purities exceeding 95%, except for CB7, which was assumed to contain 20% water. Millipore water with a conductivity of <0.05 μS was used.

2.2 Preparation of DCHALG and DCH/CB7ALG conjugates

ALG (0.4 g), DCC (~0.08 g, 0.38 mmol), and DMAP (~0.006 g, 0.049 mmol) were dissolved in DMSO nitrogen-purged for 2 h at 295 K (50 mL), and the solution was stirred for 16 h. In a separate flask, DCH (0.053 g, 0.1 mmol) or a 1:1 mixture of DCH/CB7 (0.017 g/0.037 g, 0.032 mmol) was dissolved in DMSO/water (20 mL, 1:1 v/v) upon 6-h stirring under nitrogen at 298 K. The two suspensions were mixed, and the resulting mixture was stirred for 2 h under nitrogen at 55 K and then purified by dialysis against water (pH 7) for several days to separate the solid conjugates from unreacted starting materials. The obtained suspension was then centrifuged for 8 h, and the solid product was washed with water and freeze-dried for 10 h.

2.3 Instrumentation

A Cary-300 UV−vis spectrophotometer (Agilent Technologies, Santa Clara, CA, USA) and Hellma absorption cuvettes (path length = 10 mm, volume = 3.5 mL) were used for absorbance measurements. Fluorescence spectra were recorded on a Cary-Eclipse instrument (Agilent Technologies, Santa Clara, CA, USA) using slit

widths of 2.5 nm for both the excitation monochromator and the emission monochromator in all experiments. FTIR spectra were recorded in the range of 4000–400 cm^{-1} on a NEXUS 470 FTIR instrument (GMI trusted laboratories, Ramsey, MN, USA) for samples prepared using the KBr disk method, and 512 scans were averaged for each spectrum with a spectral resolution of 2 cm^{-1}. The morphology of materials after gold coating was evaluated using a scanning electron microscope (SEM) (Inca Energy EDS System, Oxford, United Kingdom). Dynamic light scattering (DLS) and ζ-potential were recorded on a Zetasizer Nano ZS instrument (Malvern Instrumentation Ltd., Malvern, United Kingdom). NMR spectra were recorded on a 400-MHz Varian spectrometer (Varian, Inc., Palo alto, CA, USA) using tetramethylsilane as a reference, unless otherwise specified. Steady-state and time-resolved photoluminescence measurements were carried out on a LifeSpec II spectrometer (Edinburgh Inc., Edinburgh, UK) based on the time-correlated single photon counting method. Excitation (280 nm) was performed using an Edinburgh LED with a repetition rate of 20 MHz, a time resolution of 90 ps, and a red-sensitive high-speed PMT detector (Hamamatsu, H5773-04). For aqueous suspension characterization, a 305-nm long pass filter was placed between the sample holder and the emission monochromator. In the temperature variation experiment, a thermoelectrically cooled four-window cuvette holder was used together with an instrument software-powered controller to enable stable control of sample temperature from 5 to 105 K. Emission non-exponential decay traces were fitted using the Levenberg-Marquardt algorithm to minimize Chi-square. Pre-exponential factors in the decay response function were used to calculate the contribution of each lifetime component (f_i) to the entire steady-state spectra and the average excited-state lifetime (τ_{avg}) as follows:

$$f_i = \frac{\alpha_i \tau_i}{\sum_j \alpha_j \tau_j}, \tag{17}$$

$$\tau_{avg} = \sum_i f_i \tau_i. \tag{18}$$

2.4 Scanning electron microscopy

The size and morphology of DCH, ALG, DCHALG and DCH/CB7ALG was studied by using scanning electron microscope at 298 K. The average size for DCH, ALG, DCHALG and DCH/CB7ALG was calculated by using SEM resolution of 100 μm.

2.5 Particle size and size distribution

The size of the particle, and their size distribution were studied by using dynamic light scattering and zeta potential techniques. DCH, DCHALG, and DCH/CB7ALG of 0.1 mg/mL solution was prepared in water and size of the particle was studied at 298K.

2.6 Titration procedure

Two stock solutions were prepared (pH 7): (i) DCH in water (10 μM) with/without 50 μM CB7 and (ii) ANS (100 μM) in the original DCH or DCH/CB7 solution. Optical absorption and emission spectra were then recorded after the addition of aliquots of solution (ii) to a fixed volume (2.4 mL) of solution (i).

2.7 Determination of Binding Constant

The titration by using a UV-Visible spectrophotometer of DCH with CB7 was conducted to obtain the binding constant (K_a') between two CB7 macrocycles and one DCH molecule. The expression for the changes of absorbance signals (Y) as

a function of the total concentrations of CB7 ([CB7]$_0$) can be derived by considering the two equilibria below and the subsequent mass balance equations:

$$CB7 + DCH \rightleftharpoons CB7DCH$$

$$K_a = \frac{[CB7DCH]}{[CB7][DCH]} \tag{19}$$

$$CB7DCH + CB7 \rightleftharpoons (CB7)_2DCH$$

$$K_a' = \frac{[(CB7)_2DCH]}{[CB7DCH][CB7]} \tag{20}$$

The absorbance of the free DCH (Y$_{DCH}$) is:

$$Y_{DCH} = \epsilon_{DCH} [DCH]_0 \tag{21}$$

$[DCH]_0$ is the total concentration of DCH. Upon the addition of CB7 at a concentration of $[CB7]_0$, the absorbance (Y) becomes:

$$Y = \epsilon_{DCH} [DCH] + \epsilon_{CB7DCH} [CB7DCH] + \epsilon_{(CB7)_2DCH} [(CB7)_2DCH] \tag{22}$$

$\epsilon_{DCH}, \epsilon_{CB7DCH}$, and $\epsilon_{(CB7)_2DCH}$ are the molar absorptivity of DCH, CB7DCH, and (CB7)$_2$DCH , respectively.

When the signal reaches a steady value, it is assumed that only (CB7)$_2$DCH is present. The absorbance becomes:

$$Y_{(CB7)_2DCH} = \epsilon_{(CB7)_2DCH} [DCH]_0 \tag{23}$$

Mass balance equations for CB7 and DCH are:

$$[DCH]_0 = [DCH] + [CB7DCH] + [(CB7)_2DCH] \tag{24}$$

$$[CB7]_0 = [CB7] + [CB7DCH] + 2[(CB7)_2DCH] \tag{25}$$

From Eqs. 19−25 we get:

$$Y = \frac{Y_{DCH} + [CB7]_0^2 \, \in_{CB7DCH} \, K_a + Y_{(CB7)_2DCH} K_a K_a' \, [CB7]_0^2}{1 + K_a[CB7]_0 + K_a K_a' \, [CB7]_0^2}$$

In the titration experiment, the total concentration ($[DCH]_0$) was kept constant and that of the host ($[CB7]_0$) was gradually increased. Herein, we assumed the approximation ($[CB7]_0$ = $[CB7]$) is valid. The binding constant (K_a') was then determined by using the nonlinear least-squares formula of Eq. 13 for the plot of Y versus $[CB7]_0$. All parameters (K_a, $Y_{(CB7)_2DCH}$, and $\in_{CB7DCH}$ except Y_{DCH} were left unconstrained. The analysis by Levenberg-Marquardt algorithm was provided by SigmaPlot's software (version 6.1; SPCC, Inc., Chicago, Illinois, USA).

Chapter 3: Results and Discussion

3.1 Interaction of DCH with CB7 in solution

Changes in the NMR signals of DCH upon the addition of 0.2 equiv. of CB7 indicated that the macrocycle shuttles (see also temperature dependent NMR results) along the guest's alkyl chain stalk while leaving the aromatic portion outside the cavity (Figure 10), as has been reported for similar cationic guests.[25−28] The inclusion pattern was inferred from the splitting of alkyl (a, b, and c), methyl, and aromatic (d and e) proton signals into two sets of peaks at lower and higher ppm compared to those of DCH in D_2O. To elaborate on the interaction of the aromatic protons with CB7, the NMR spectra of DCH were measured upon the addition of several equivalents of CB7 (see Figure S1 in Appendix, page 58-59). The assigned aromatic signals (e_1, e_2, e_3, e_4), were not equally shifted to higher ppm upon complexation to CB7. The variation in this shift suggests a diverse interaction of the aromatic portion with the CB7 cavity as illustrated in the cartoon representation of the $(CB7)_2DCH$ complex, which is depicted in (Figure S1 in Appendix, page 58-59).
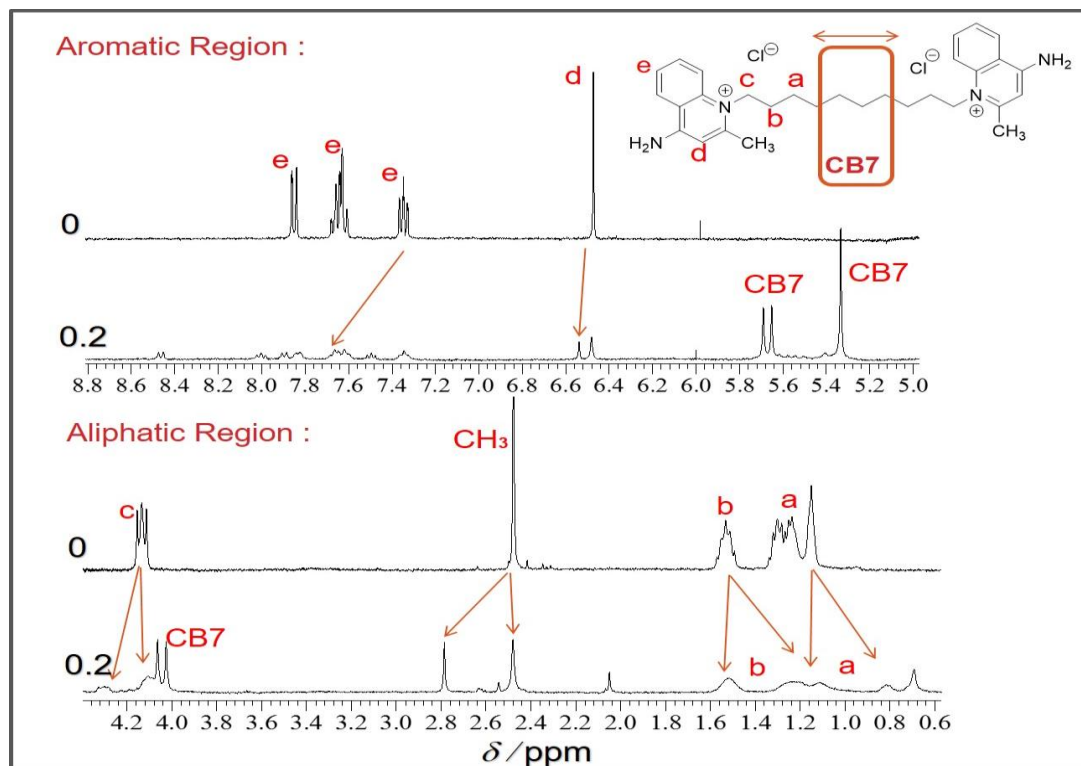
Figure 10: ^{1}H NMR spectra of DCH (1.5 mM) with CB7 (0.3 mM; 0.2 equiv.) in D$_2$O with pD 7.0 (400 MHz).

DCH peaks were assigned based on a previous report.[17] NMR titration of DCH with CB7, the Job's plot data (see Figure S2 in the Appendix, page 60-62) supported a 2:1 host−guest stoichiometric binding and suggested that when 2 equiv. of CB7 are added to the DCH solution (DCH/CB7 molar ratio = 0.3), each CB7 ends up at any of the two protonated aromatic rings of DCH, mostly engulfing protons a (see Figure S1 in the Appendix, page 58-59).
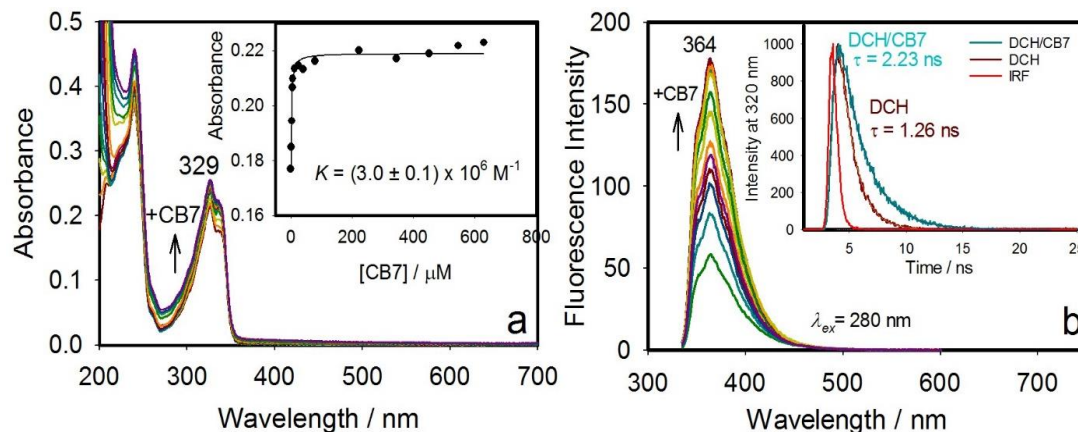
Figure 11: Effects of CB7 addition (0−60 equiv.) on the UV−vis absorption (a) and emission (b) spectra of DCH (10 μM) at pH ~7 and 298 K. Insets in (a) and (b) show the corresponding titration curve and single-exponential emission decays for DCH in the presence and absence of CB7 (50 equiv.), respectively. The inset shows the nonlinear fitting to a 2:1 CB7:DCH binding model solid line

The interaction of DCH (10 μM) with CB7 (0−60 equiv.) was confirmed in solution at pH 7 by UV−vis absorption titration (Figure 11a), and UV−vis absorption data at 329 nm indicated very strong binding between DCH and CB7. Upon CB7 addition, absorbance signals gained intensity and shifted to lower wavelengths, while steady-state emission signals at 364 nm (excitation at 280 nm) became more intense (~three-fold) but retained their position (Figure 11b). The isosbestic point observed at ~350 nm was indicative of a host-guest equilibrium. These UV-visible spectral changes in the region between 300 and 400 nm confirm the interaction of the aromatic portion of DCH with CB7 (see also NMR results). The titration data were fitted to a non-linear equation, which was obtained from assuming a 2:1 binding equilibrium between CB7 and DCH with a correlation coefficient of R equals to 0.99 and a binding constant (K_a') equals to $3.0 \pm 0.1 \times 10^5$ M^{-1}.

Similar results were obtained when emission was monitored at other wavelengths (see Figure S3a in the Appendix, page 63). Changes of DCH excitation wavelength affected the intensities of emission spectra but did not affect emission peak positions (see Figure S3b in the Appendix, page 63). Figure 11b shows that the three-fold CB7-induced fluorescence enhancement was accompanied by a 1.5-fold increase in the excited-state lifetime from 1.26 to 2.23 ns. The single-exponential lifetime, observed at all wavelengths across the emission spectra of DCH (10 μM) or DCH/CB7 (5 equiv. of CB7), was explained by considering excitation and excitation-dependent emission spectra. Thus, the restoration of the violet emission of DCH at 364 nm upon complexation with CB7 was ascribed to the suppression of collisional quenching by chloride ions.[33]

3.2 Energy transfer from DCH to ANS in solution

As a control experiment, we confirmed the spectral overlap $(J)^2$ between the violet emission of DCH and the absorbance of ANS (Figure 12a), demonstrating that no interactions between ANS and DCH in the ground state were observed both in the absence (Figure 12b) and presence (5 equiv., Figure 12c) of CB7. Moreover, the very weak absorption of ANS at 270-340 nm precluded its direct excitement in this range. No changes in the spectral profile of ANS (Figure 12d) in this and other ranges were observed upon CB7 addition, which confirmed the lack of interaction between CB7 and ANS in the ground state. Additionally, no changes in the absorbance of DCH at 280 nm were observed upon CB7 addition (Figure 11a). Thus, we concluded that at 280 nm, only DCH fluorophores were excited upon mixing with ANS in the absence or presence of CB7.
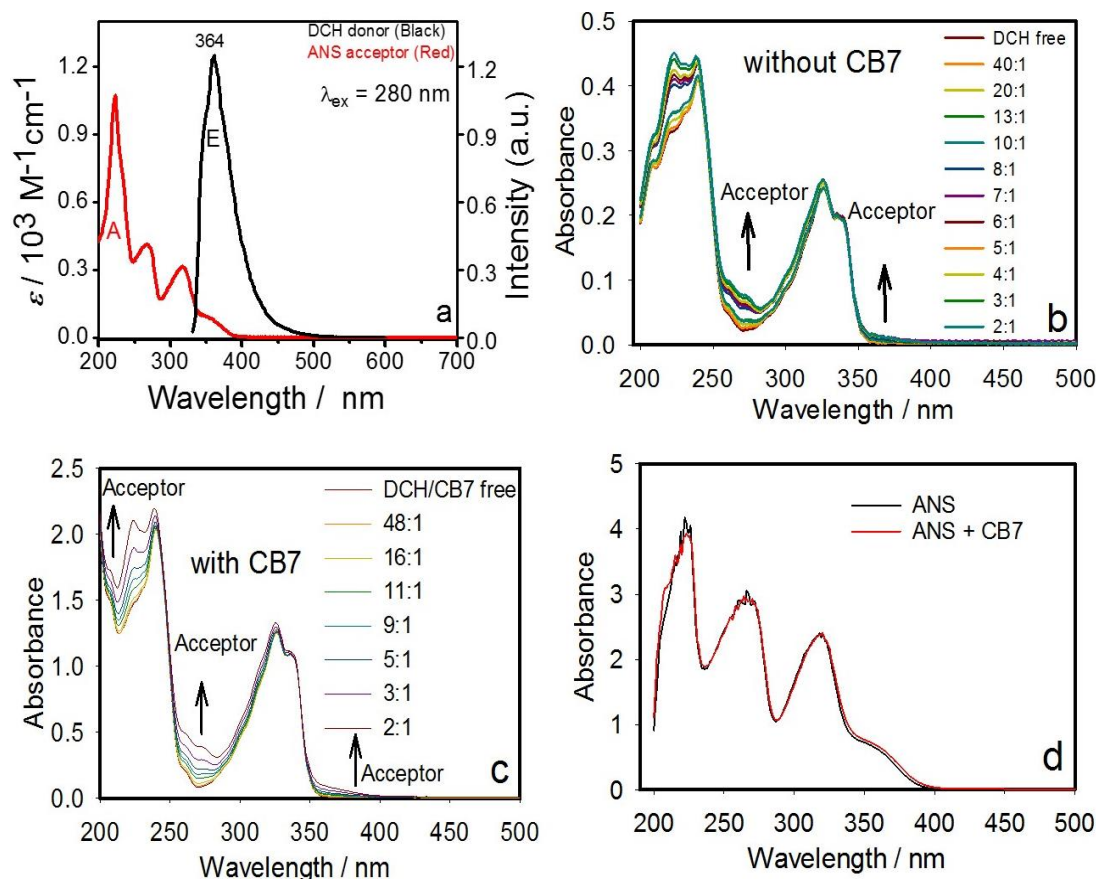
Figure 12: Spectral overlap between DCH (black spectra) (a) and ANS (red spectra) (b) in aqueous solution. A and E labels denote absorption and emission spectra, respectively. UV−vis absorption spectral changes of DCH (10 μM) for different DCH/ANS ratios in the (b) absence and (c) presence (5 equiv.) of CB7. (d) Absorption spectra of ANS (40 μM) in the presence of CB7 (360 μM).

The fluorescence titration of DCH with ANS at different DCH/ANS ratios was accompanied by weak energy transfer from violet to blue (Figure 13a), whereas much more efficient energy transfer was observed in the presence of CB7 (5 equiv., Figure 13b) as CB7 assist energy transfer from donor to acceptor. The spectra shows the evolution of new peaks at 450 nm from the band at 300 nm only in the presence of CB7. The substantial decrease in the lifetime (in the presence of CB7) provides better evidence for the occurrence of FRET.
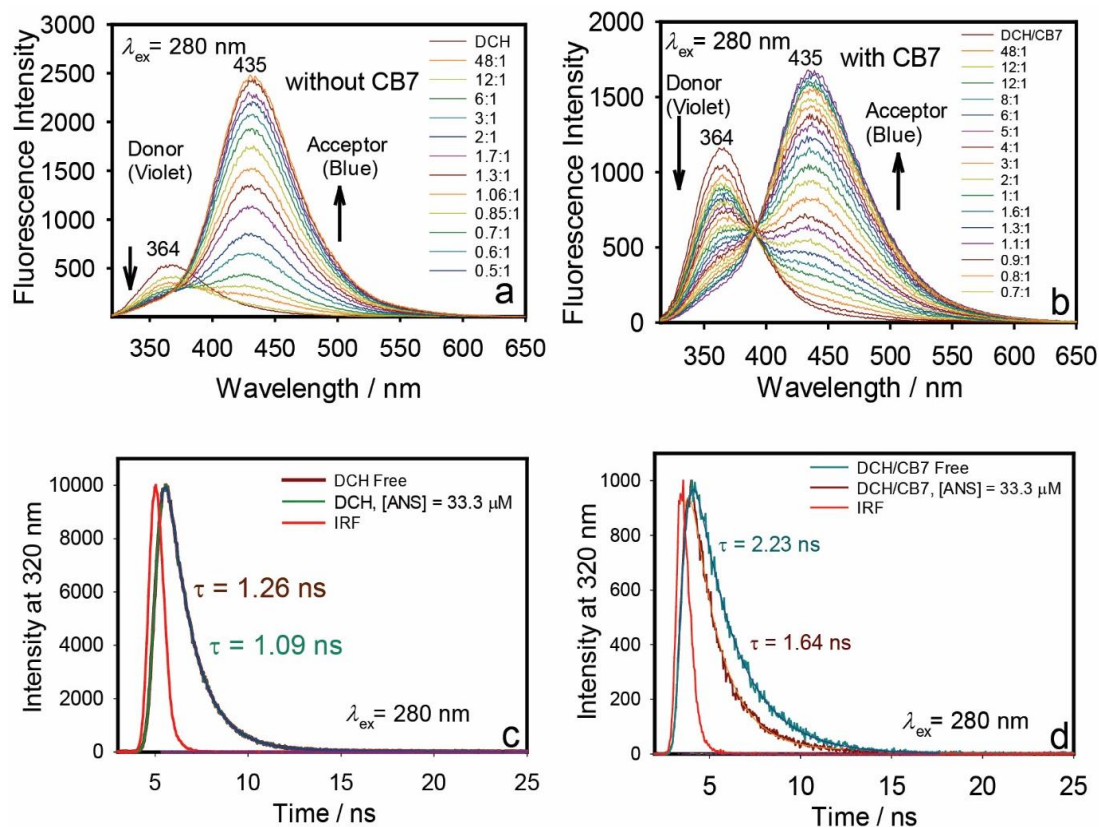
Figure 13: Energy transfer from DCH to ANS in solution illustrated by changes in the emission spectra and decays of DCH (10 μM) 320-nm emission intensity at different DCH/ANS molar ratios in the absence (a, c) and presence of CB7 (b, d) at 298 K.

The occurrence of FRET between the two fluorophores (DCH and ANS) was confirmed by time-resolved photoluminescence measurements,[12,34−38] i.e., decays of DCH 320-nm emission upon laser diode source–induced excitation at 280 nm were collected. The excited-state lifetime of DCH in Table 1 (Figure 13c) decreased from 1.26 to 1.09 ns in the absence of CB7, whereas CB7-assisted energy transfer from DCH to ANS in Table 2 (Figure 13d) resulted a more substantial decrease from 2.23 to 1.64 ns. The occurrence of FRET in cases when the excited-state lifetime of a donor decreases upon the addition of an acceptor has been confirmed for several supramolecular light harvesting systems.[12,34−38]

The decay of DCH emission induced by the addition of 2 equiv. ANS changed from single-exponential to double-exponential in the presence of 5 equiv. CB7 (compare Table 1 and Table 2), and the origin of the new lifetime component was probed by emission titration of ANS with CB7 (see Figure S4 in the Appendix, page 68). The addition of 2 equiv. of CB7 to ANS did not significantly change the intensity or position of the ANS emission peak at 475 nm (Figure S4 in the Appendix page 68, excitation at 370 nm), and the new lifetime component was attributed to the formation of an ANS/CB7 complex in the excited state.[30] Therefore, at ANS concentrations above 20 μM, the average lifetime was considered (Figure 10d).

Table 1: Excited-state lifetime constants observed at 320 nm for DCH (10 mM) in water at different concentrations of added ANS at 298 K. The calculated Förster radius (R_0) is also shown at each set of data points.

[ANS] / μM	T	R_o	χ^2
0	1.26		0.831
0.21	1.27	188	1.015
0.83	1.26	158	1.026
1.64	1.27	139	1.047
2.83	1.25	170	1.203
4.00	1.22	176	1.321
5.88	1.21	189	1.254
7.69	1.15	200	1.502
9.77	1.18	184	1.519
11.8	1.13	190	1.697
14.3	1.14	178	1.464
17.2	1.13	175	1.725
20.0	1.11	162	1.672
25.0	1.09	157	1.731
33.3	1.09	150	1.824

Time resolution was ~90 ps and the excitation wavelength was at 280 nm. Lifetime values are presented as mean ± standard deviation. The estimated experimental error was 2% for the single exponential lifetimes. R_0 has an arbitrary unit as defined in FAST software (see Experimental Section).

Table 2: Excited-state lifetime constants along with the average lifetimes (see the Experimental Section) observed at 320 nm for DCH/CB7 (10 μM for DCH and 50 μM for CB7) in water at different concentrations of added ANS at 298 K. The calculated Förster radius (R_0) is also shown at each set of data points.

[ANS] / μM	τ_1/ ns	τ_2/ ns	τ_{avg}/ ns	R_o	χ^2
0.00	2.23		2.23		0.983
0.21	2.21		2.21	229	1.049
0.83	2.21		2.21	200	1.217
1.20	2.19		2.19	158	1.043
1.80	2.21		2.21	158	1.105
2.40	2.20		2.21	167	1.112
3.20	2.18		2.18	159	1.046
4.00	2.16		2.16	167	1.132
5.10	2.13		2.13	177	1.102
6.30	2.15		2.15	155	1.105
7.70	2.12		2.12	164	1.203
9.10	2.09		2.09	162	1.042
10.4	2.10		2.10	164	0.963
12.4	2.06		2.06	169	1.404
14.3	2.01		2.01	169	1.340
16.1	1.97		1.97	172	1.340
17.8	1.94		1.94	177	1.258
20.0	1.92		1.92	179	1.397
22.1	0.76	2.18	1.82	173	1.012
24.1	0.82	2.26	1.80	174	1.095
25.5	0.79	2.25	1.75	177	0.981
27.7	0.71	2.10	1.70	176	0.960
29.4	0.81	2.18	1.67	180	1.152
33.3	0.88	2.31	1.64	179	1.010

Time resolution was ~90 ps and the excitation wavelength was at 280 nm. Lifetime values are presented as mean ± standard deviation. The estimated experimental error was 2% for the lifetime around 1 ns and 20% for the lifetime around 2 ns. R_0 has an arbitrary unit as defined in FAST software (see Experimental Section).

The selective excitation of DCH at 280 nm (see above) allowed us to calculate the rate of intermolecular (bimolecular quenching) energy transfer (k_T) using classical chemical kinetics. It was assumed that some DCH molecules absorb photons generated by the very short pulse of light at time zero to afford excited state S_1 and then return to ground state S_0 either radiatively (k_r) or non-radiatively (k_{nr}). Alternatively, rapid

FRET quenching (k_T) of DCH emission with ANS as the acceptor occurs. The k_r and k_{nr} deactivation pathways of DCH fluorophores are assumed to be equivalent in the absence and presence of CB7. The k_T values of 4.07×10^{12} M^{-1} s^{-1} for DCH + ANS (linear correlation coefficient $R = 0.91$) and 4.91×10^{12} M^{-1} s^{-1} ($R = 0.98$) for DCH/CB7 + ANS were obtained from the slopes of Stern-Volmer plots (K_{SV}) (Figure 11a), which present the unquenched lifetime (τ_0)/quenched lifetime (τ) ratio as a function of ANS concentration in water.[31]
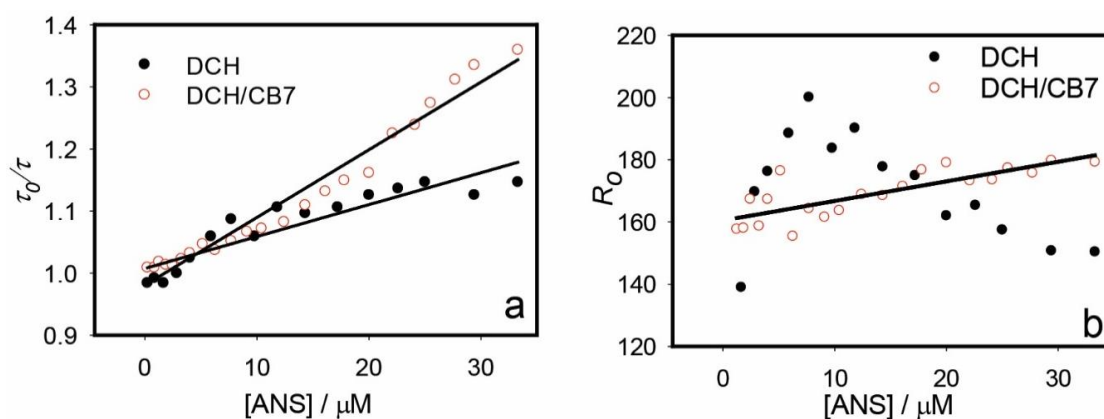
Figure 14: Stern-Volmer plots for the quenching of DCH (10 μM) emission at 298 K. in the presence and absence of CB7 (50 μM) at different ANS concentrations (a). Förster radius (R_0) (b) estimated by FAST software (Edinburgh, version 3.4.0) as a function of ANS concentration in the presence and absence of CB7.

However, k_T at 298 K was calculated as 8.27×10^9 M^{-1} s^{-1}. The non-proximity of the two experimental and theoretical values confirms that the FRET process is not diffusion-controlled.[10] k_T was calculated based on Smoluchowski (Eq. 26) and Stokes-Einstein (Eq. 27) relations assuming a pure diffusion-limited process (k_d).[40]

$$k_T = k_d = 4\pi N R_q D, \tag{26}$$

where R_q is the closest-approach distance (m), D is the mutual diffusion coefficient (m^2 s^{-1}), and $N = 1000N_a$ (N_a = Avogadro's number). D is the sum of the translational diffusion coefficients of the fluorophore (DCH) and quencher (ANS), D_M and D_Q, respectively, and can be expressed by the Stokes-Einstein relation (Eq. 27):

$$D = D_M + D_Q = \frac{\kappa T}{6\pi\eta}\left(\frac{1}{R_M} + \frac{1}{R_Q}\right)_{,} \tag{27}$$

where κ is Boltzmann's constant (1.381×10^{-23} kg m^2 s^{-2} K^{-1}), η is the viscosity of the medium ($\eta = 8.95 \times 10^{-4}$ kg m^{-1} s^{-1} for water at 298 K),[40] and $R_M = 10 \times 10^{-10}$ m and $R_Q = 5 \times 10^{-10}$ m are the hydrodynamic radii of the hydrated fluorophore (DCH) (roughly estimated using ChemDraw software) and hydrated quencher (ANS),[41] respectively.

In Figure 14b, a theoretical kinetic model of FAST software (version 4.3.0) was utilized to estimate the Förster radius (R_0) (see Figure S5 in Appendix page 69-70). As all ANS acceptor dipoles were randomly distributed around DCH donor dipoles, no diffusion was allowed to occur during the DCH excited-state lifetime. The model also assumed that species were distributed in a rigid 3-D solution, i.e., that DCH molecules did not interact with themselves. The corresponding fits of Förster kinetics for DCH/CB7 with ANS and DCH with ANS are shown in (Figure S5 in the Appendix, page 69-70) and (Figure S6 in the Appendix, page 71-72) respectively. In our analysis, we kept τ_0 fixed while estimating the characteristic constant Γ, a floating parameter. Γ and ANS concentration were then substituted into the given equation by FAST software (Eq. 28) to estimate R_0.

$$R_0 = \sqrt[3]{\frac{447\Gamma}{[ANS]}} . \tag{28}$$

Data in Figure 14b support the validity of our model only in the presence of CB7 for ANS concentrations of 1.20–33.3 μM with mean value ± standard deviation of $R_0 =$ 169 ± 7.

3.3 Covalent attachment of DCH and DCH/CB7 to alginate carbohydrates

As the occurrence of FRET from DCH to ANS was only confirmed in solution, we decided to extend the results to ALG carbohydrate platforms. A similar attachment of DCH to chitosan was reported during the preparation of this manuscript.[17] The formation of an amide linkage between DCH and ALG (Scheme 1) realized by a previously reported procedure[42,43] (see Experimental Section) was confirmed by FTIR spectra of DCH, ALG, and the DCHALG conjugate formation was confirmed by FTIR using the KBr disk. The amide linkage formation was also confirmed by corresponding NMR spectra recorded in a 1:1 (v/v) mixture of D_2O and DMSO-d_6 (See Figure S7 in Appendix, page 73-74).
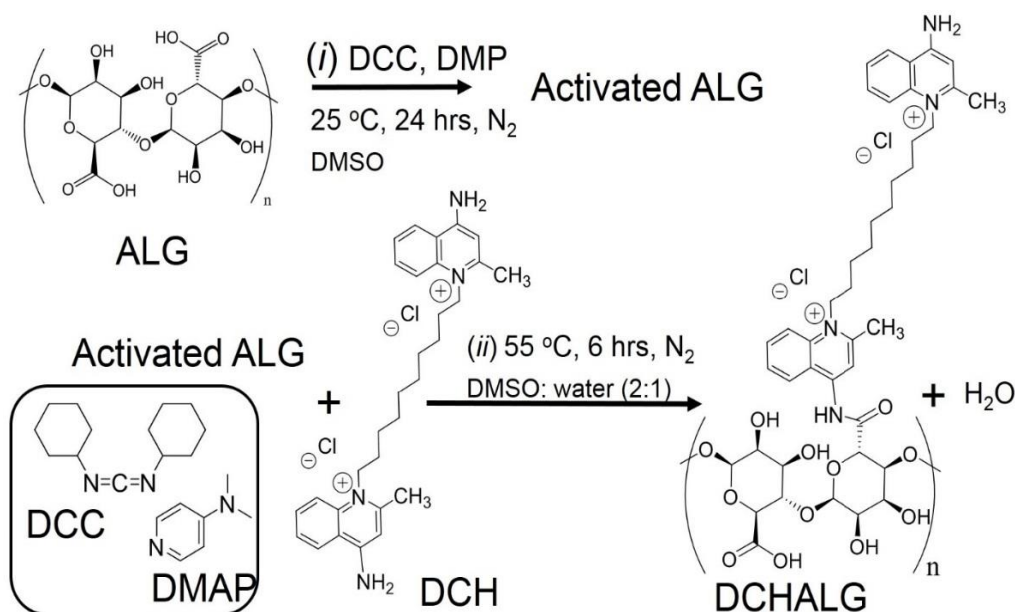
Scheme 1: Procedure used for the covalent attachment of DCH to ALG.

3.4 Characterization of polymers by FTIR

The NH signal at 3500 cm^{-1} in the FTIR spectra of DCH totally disappeared upon conjugation to ALG in both the presence and absence of CB7, while the C=O stretching peak of alginic acid shifted to lower frequencies (from 1700 to 1650 cm^{-1}) because of the formation of an amide linkage (CONH) between DCH (NH$_2$ group) and alginic acid (COOH group) as shown in Figure 15. No clear shift of FTIR peaks was associated with the formation of DCH/CB7ALG. As a summary the NH signal at 3500 cm^{-1} in the FTIR spectra of DCH and the C=O stretching peak of alginic acid shifted to lower frequencies (from 1700 to 1650 cm^{-1}) disappear in both the conjugate with and without CB7 that confirms the formation of two new conjugates.
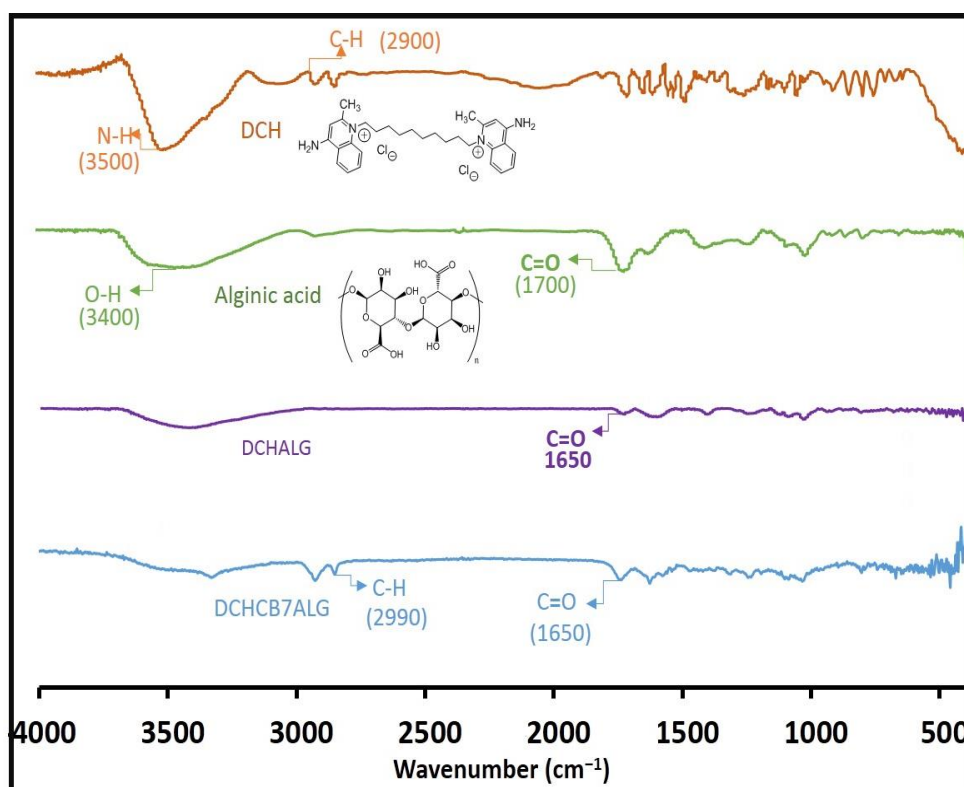

Figure 15: The Fourier-transform infrared (FTIR) spectra in KBr desk for different solids, as indicated in the figure.

3.5 Characterization of polymers by NMR

DCHALG and DCH/CB7ALG polymer was further characterized by NMR as shown in Figure16. The comparison of proton NMR resonances in Figure 16 and (see Figure S7 in Appendix, page 73-74) for DCHALG and DCH/CB7ALG in D_2O:DMSO-d_6 (1:1, v/v) confirmed the shuttling of CB7 along the alkyl stalk in analogy to the NMR results in solution. Closer look at the NMR spectrum of the supramolecular polymer DCH/CB7ALG also reveal the splitting of the aromatic (d) proton signals into two sets of peaks at lower and higher ppm and the shifting of the alkyl (a and b) proton signals to lower ppm in comparison to those of DCHALG polymer in D_2O/DMSO-d_6 solvent mixture. Moreover, the significant broadening and shifting of the NMR peaks that correspond to the aromatic (e) proton signals to higher ppm also indicate interaction of both aromatic terminals with CB7 by analogy to the results in solution upon the addition of two equivalents of CB7. In general, the formation of a totally new structure caused by covalent conjugation was confirmed by the appearance of new distinct NMR patterns for each sample, in line with the observation of new NMR patterns of DCH upon conjugation to glycol chitosan.[17]
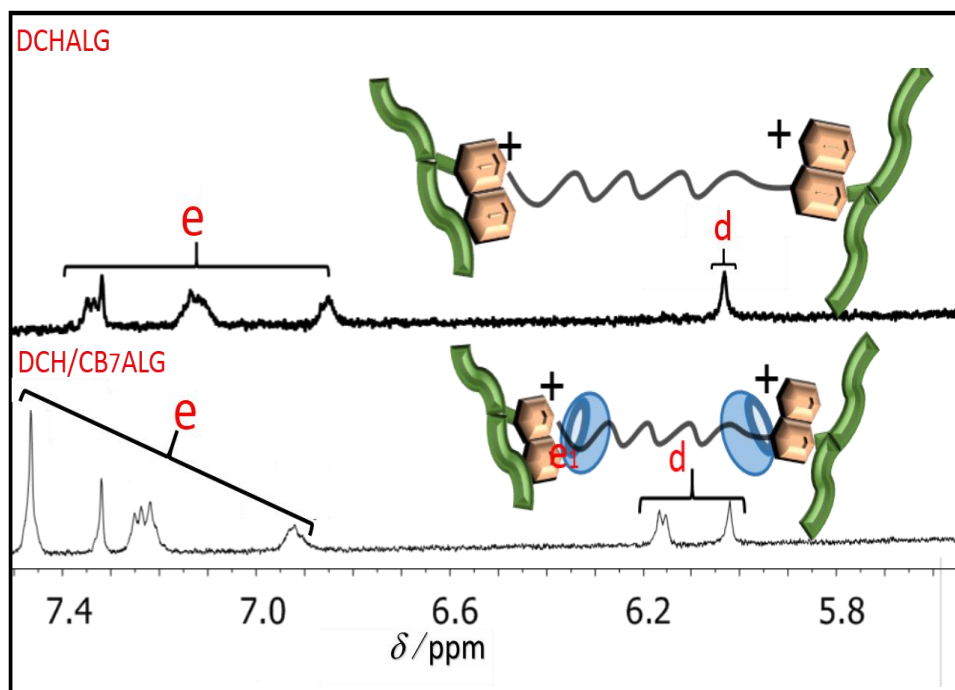
Figure 16: ^{1}H NMR spectra of DCHALG and DCH/CB7ALG (280 mg/mL) in D$_2$O/DMSO-d$_6$ (1:1) with pD ~7.0 (500 MHz) at 298 K.

3.6 Characterization of polymers by DLS

The particle size distribution and surface charge of ALG, DCHALG, and DCH/CB7ALG polymers (0.1 mg/mL) were studied by Dynamic Light Scattering (DLS) as shown in Figure 17. The measurements for ALG (Figure 17a) show bimodal size distribution and the presence of large or sedimenting particles with bimodal peaks of 8.5 and 202.8 nm, which is a result of agglomeration.[44] Figure 17b shows the size and size distribution of the particles for DCHALG (284 nm, single peak). Coagulation and the subsequent sedimentation of the agglomerated particles upon formation of DCHALG polymers indicate good binding of DCH to ALG. On the contrarily, Figure 17c, which illustrates the size measurement for DCH/CB7ALG, shows a trimodal distribution and a presence of large particles (330 nm) along with smaller ones (24 and 6 nm). The appearance of large and small particles could be attributed to the interaction

of DCH with CB7. The ζ-potential of DCH/CB7ALG supramolecular polymers (0.1 mg/mL) was determined to be -0.0453 mV, which shows a reduction of negative surface charge compared to that of DCHALG polymers (- 0.191 mV) because of host-guest interaction. The higher value of the ζ-potential for ALG alone (-0.705 mV) compared to that of DCH/CB7ALG polymers could also be attributed to the low-to-no motion of the particles and the formation of big agglomerates (see also SEM results). PDI is a parameter used to describe the degree of non-uniformity of a size distribution of particles. The results show relatively high PDI values: 0.551, 0.152, and 0.474 for ALG, DCHALG, and DCH/CB7ALG, respectively. However, the values fall within an acceptable range.[45].
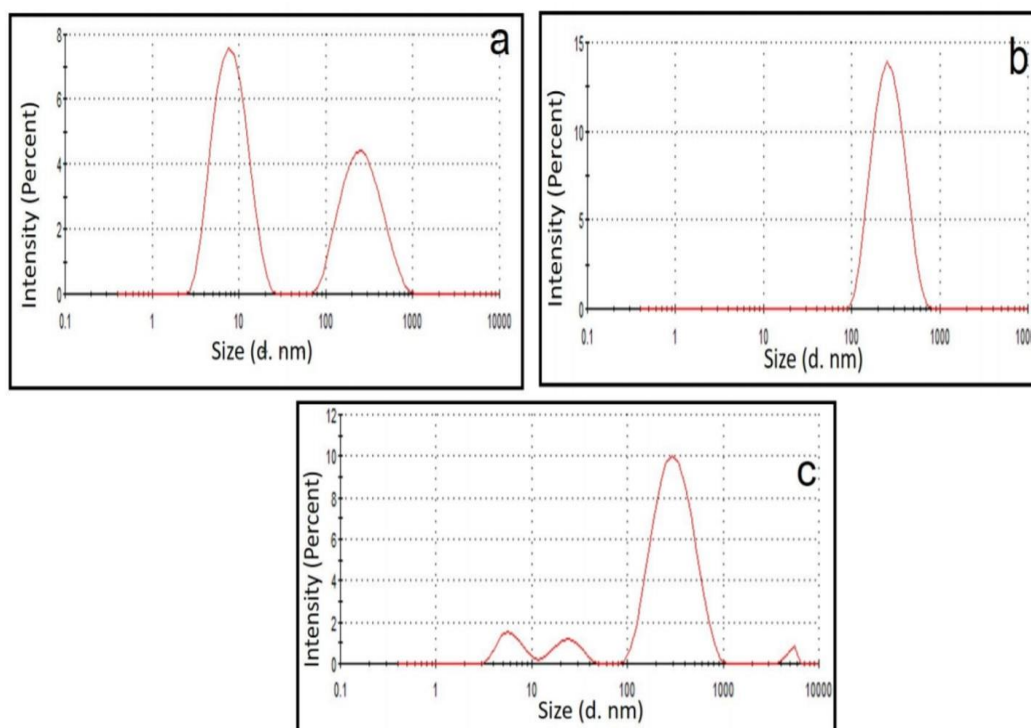
Figure 17: Size distributions for ALG (a), DCHALG (b), and DCH/CB7ALG (c) measured by using DLS technique for 0.1 mg/mL concentration in 0.1 M NaCl solutions at 298 K.

3.7 Characterization of polymers by SEM

The newly synthesized conjugate with and without CB7 was further characterized by scanning electron microscopy (SEM). The Figure 18 shows SEM micrographs for ALG (a), DCH (b), DCHALG (c), and DCH/CB7ALG (d). Results indicate that both the original and fabricated DCHALG polymers are composed of aggregated particles. However, DCH/CB7ALG polymer characterized by rode-shape particles with a range average of 10 μm diameter has a distinct morphology, which differs from fully bulky chunks for DCHALG polymer. The variation of surface morphology can be attributed to the threading of CB7 onto the DCH backbone upon grafting onto ALG polymers

Figure 18: Representative SEM micrographs for ALG (a), DCH (b), DCHALG (c), and DCH/CB7ALG (d). Average particle size was 40, 18, and 10 μm for ALG, DCH, and DCH/CB7ALG, respectively.

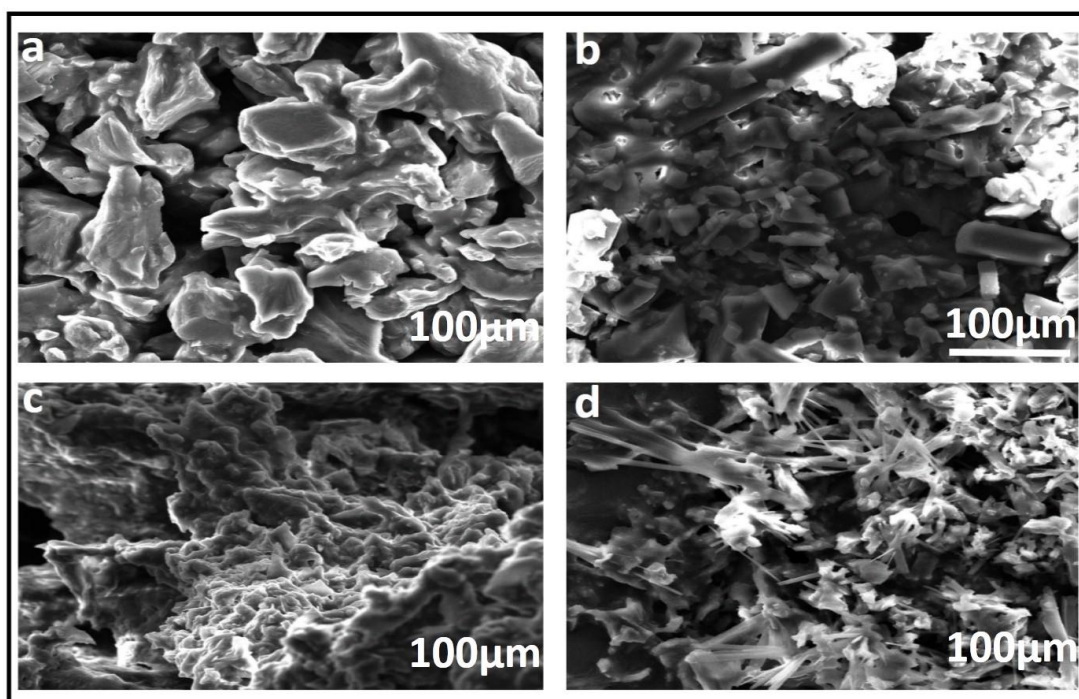The spectral and photophysical properties of DCH dramatically changed (Figure 19) upon the attachment of the free or CB7-complexed dye to ALG at 298 K, as exemplified by the emergence of new absorption and emission spectral profiles (intensity and position) for the new conjugates in aqueous suspensions. The main absorption peaks shifted to lower wavelengths upon conjugation, namely from 329 nm (DCH) to 280 nm (DCHALG) and 260 nm (DCH/CB7ALG) (Figure 19a). The emission maximum of the DCHALG conjugate (aqueous suspension, 405 nm) was red-shifted compared to that of DCH in aqueous solution (364 nm; Figure 19b). Comparison of the emission decay trace of DCH/CB7ALG with that of DCHALG aqueous suspension at 298 K (Figure 19c) showed that CB7 induced an almost 10-fold fluorescence intensity enhancement, a blue shift (from 405 to 387 nm, Figure 19b), and a two-fold increase in the average excited-state lifetime (from 2.13 to 4.43 ns). These changes were attributed to the non-radiative rate low that DCH experiences a less polar environment upon the addition of CB7 when adsorbed onto ALG.[40] The emission decays for the two conjugates at 320 nm upon excitation at 280 nm were best fitted by double-exponential (DCHALG) and triple-exponential (DCH/CB7ALG) functions, with the corresponding average excited-state lifetimes at 298 K summarized in Tables S1 and S2 in Appendix page 64-65.
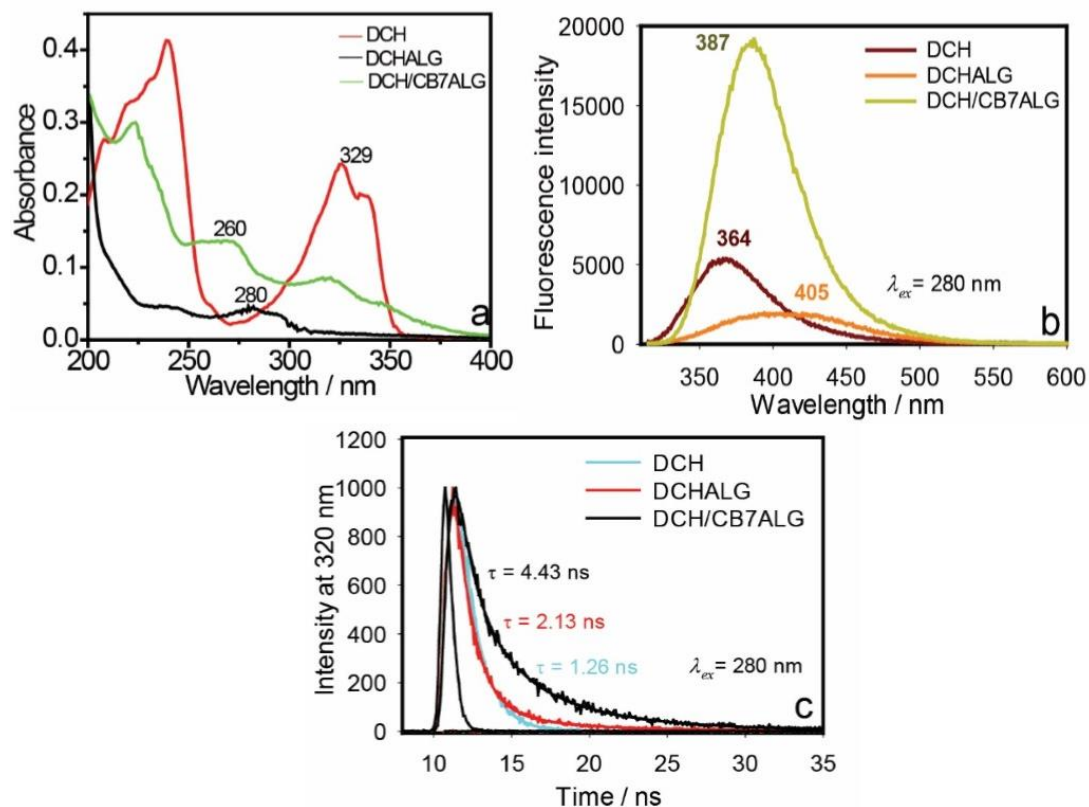
Figure 19: UV−vis absorption (a) and (b) emission spectra as well as (c) 320-nm emission decays of DCH (10 μM aqueous solution). DCHALG (1.5 mg/L aqueous suspension), and DCH/CB7ALG (2.75 mg/L aqueous suspension). In (c), the decay trace for DCH at 320 nm is added for comparison.

The conditions for energy transfer (spectral overlap and excitation at 280 nm) from the donor (DCH/ALG or DCH/CB7ALG) to the acceptor (ANS) in aqueous suspensions were confirmed analogously to the solution-phase case (see Figure S8 in Appendix, page 75).
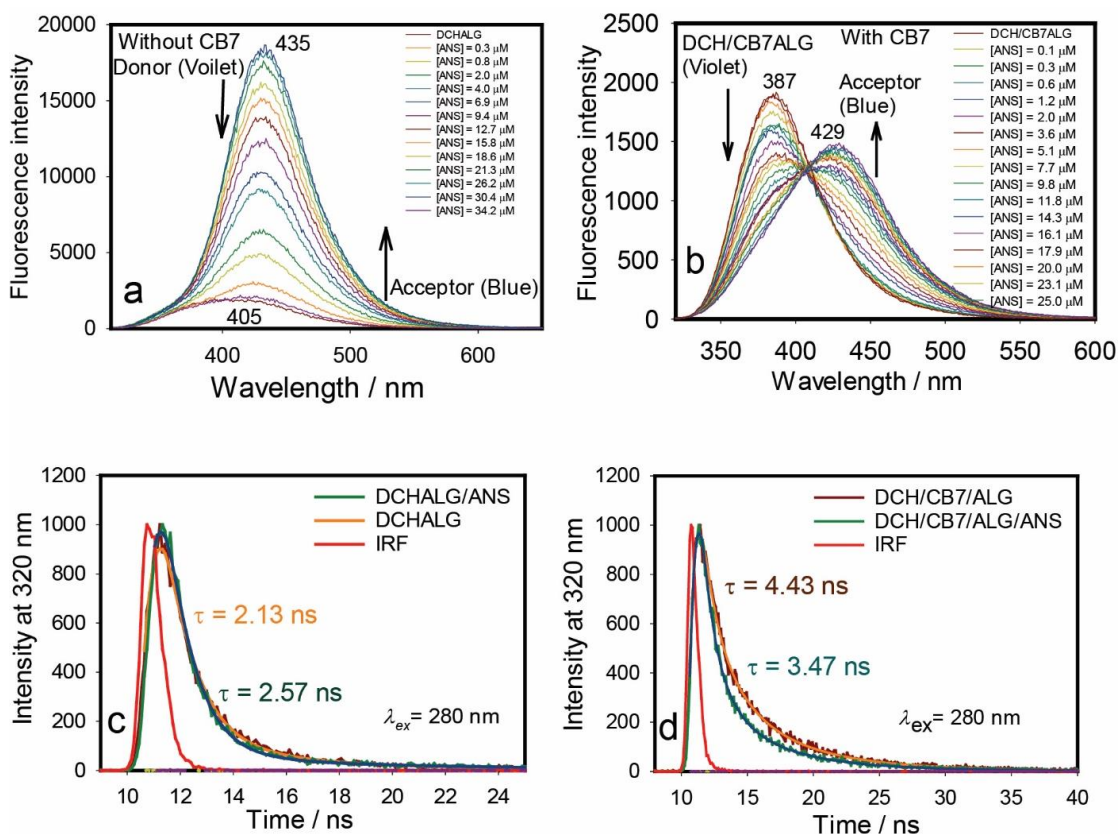
Figure 20: Energy transfer from (a) DCHALG (1.5 mg/L aqueous suspension) and (b) DCH/CB7ALG (2.75 mg/mL aqueous suspension) to ANS at different concentrations. Corresponding 320-nm emission decays labeled by the calculated average excited-state lifetime (Tables S3 and S4) (c) in the absence and (d) in the presence of CB7.

The host-assisted enhancement of the efficiency of energy transfer between DCH and ANS upon DCH linking to the ALG platform was confirmed by the decrease in the excited-state lifetime at 320 nm from 4.43 ± 0.4 to 3.47 ± 0.4 ns in the presence of CB7 (Figure 20), while a slight increase from 2.13 ± 0.4 to 2.57 ± 0.4 ns was observed in the absence of CB7. Based on the corresponding Stern-Volmer plot in Figure 21a, k_T was calculated as 1.14×10^{12} M^{-1} s^{-1} for DCHCB7/ALG + ANS ($R = 0.96$) at 298 K, which was indicative of a non-diffusion-controlled process. In Figure 21b, the theoretical kinetic model of FAST software (version 4.3.0) used to estimate R_0, was only valid in the range of ANS concentrations from 16.1 to 33.3 μM. The

obtained mean value $\pm$ standard deviation of 209 ± 9 exceeded that calculated in solution and also indicated a non-diffusion-controlled process.
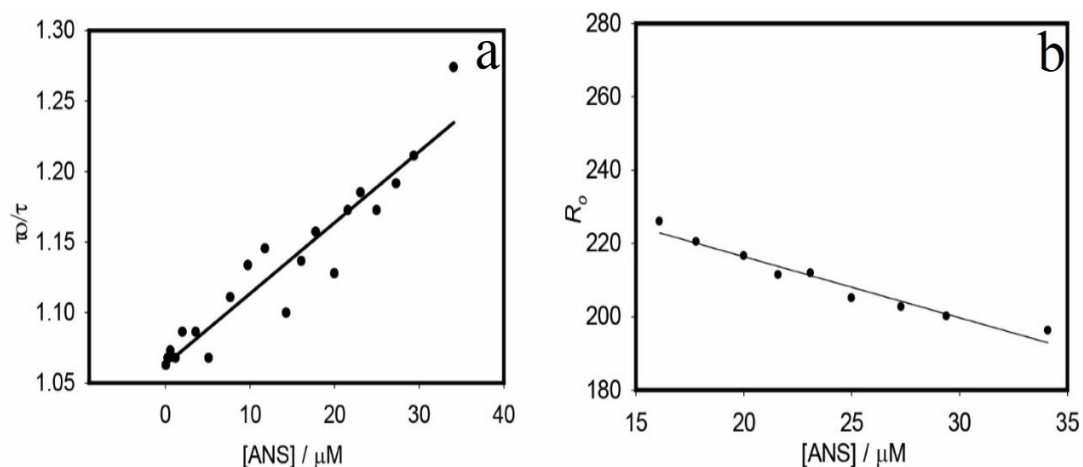
Figure 21: The Stern-Volmer plots for the quenching of the emission of DCH/CB7ALG (2.75 mg/L, water suspension) at different [ANS] concentrations(a). The plot of the estimated Förster radius (R_0) (b) utilizing FAST software (Edinburgh, version 3.4.0) as a function of [ANS] concentrations from 16 to 33 μM.

3.8 Implication for temperature sensing

Following the fabrication of the above DCH/CB7ALG, we checked if control of the surrounding environment temperature allowed us to modulate FRET in aqueous suspensions. An experimental support for the shuttling of CB7 is inferred from the temperature dependent NMR spectra (see Figure S9 in Appendix, page 76-78), which were collected for the supramolecular carbohydrate polymers (DCH/CB7ALG) at 298 K and 338 K. The results clearly illustrate the substantial evolution of the NMR signals upon increasing the temperature in a manner, which reflects faster shuttling within NMR time scale upon increasing the temperature. Noticeably, the doublet of the e_1

proton is mostly affected by the temperature variation when compared to other e

protons. It becomes less broaden at higher temperature. In addition, the aliphatic peaks

(a, b, and c) become more resolved upon increasing the temperature, which also

suggests faster shuttling. The peaks attributed to CB7 at 4.2 and 3.9 ppm were used to

estimate the CB7/DCH ratio within the polymer. The results suggest that each DCH

stalk is engulfed by two macrocycles. To ensure the integrity of our inspection prior

to any emission measurements, we first initiated energy transfer by adding 0.5 μM

ANS at 298 K. Subsequently, temperature was decreased to 278 K, raised to 378 K,

and lowered back to 278 K as shown in Figure 22. The process was repeated three

times after ANS addition using an ANS concentration increment of 2.75 μM per cycle

(up to 8.75 μM).

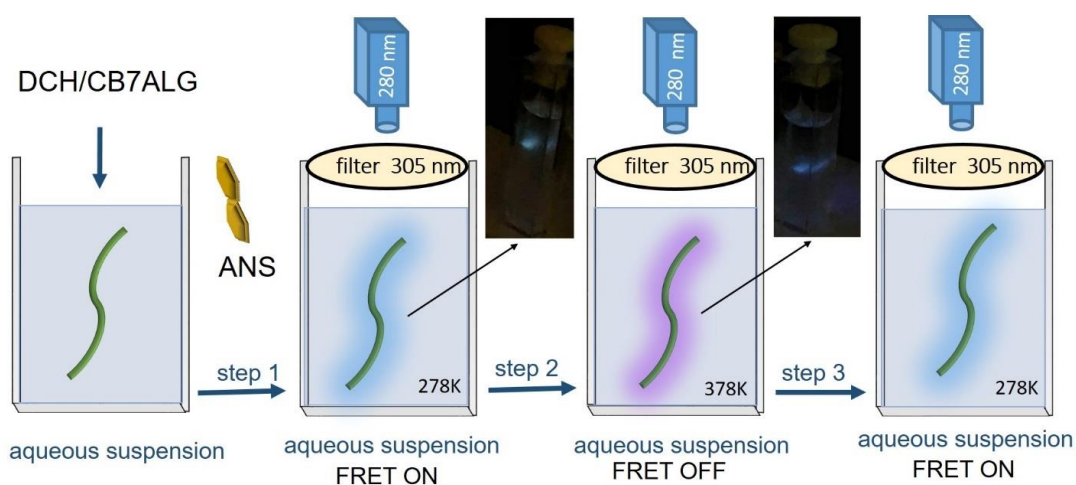Figure 22: Schematic representation of FRET signal regeneration in aqueous suspensions. Step 1: Induction of energy transfer (FRET ON) from DCH/CB7ALG (2.75 mg/L) to ANS via addition of an incremental amount of ~7 μM ANS. Step 2: Increase of temperature from 278 to 378 K to switch off the FRET signal. Step 3: Temperature decrease from 378 to 278 K to restore the FRET signal. Five cycles were generated in total.

While collecting emission data, we followed the procedure in Figure 22. The results in Figure 22 confirm the reversible response of DCH/CB7ALG to the change in temperature from 278 to 378 K upon four-fold addition of an incremental amount of ANS (~7 μM, from ~8.75 to 33.3 μM) to generate five sensing cycles. The results confirmed the responsiveness of the new supramolecular polymers to thermal stimuli at 298–368 K in aqueous media. It must be noted that in Figure 23, the unquenched/quenched lifetime ratio (τ_o/τ) in each cycle was measured upon only switching the temperature from 298 to 368 K. Moreover, we measured the excited-state lifetime instead of the steady-state spectra, as the former was better suited for the validation of FRET signal modulation in response to a thermal stimulus. In Figure 23, a decrease in the FRET efficiency was observed, even within the experimental error of the lifetime because two extreme temperatures have been used 278K and 342K. In real life application, the range of temperature may not exceed 293-313K.
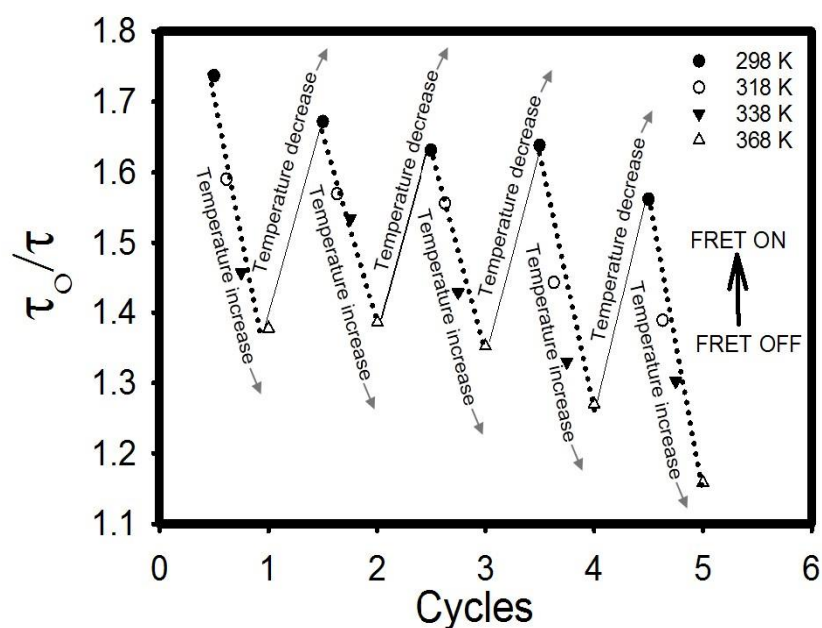

Figure 23: On/off switching of FRET signals between 298 and 368 K in 20-K steps monitored by the increase of the unquenched/quenched lifetime ratio upon temperature decrease (FRET ON) and increase (FRET OFF).

Putting it all together, when DCH (donor) in DCH/CB7ALG was excited at 280 nm in the presence of ANS (acceptor), a decrease in its emission at 387 nm was accompanied by an increase in emission at 429 nm only in the presence of a confined pocket (CB7), which confirms the occurrence of energy migration via FRET. Thus, encapsulation by CB7 led to more efficient energy transfer from DCH to ANS and caused a color shift from violet to blue. The emission of the prepared supramolecular polymer could be controlled by changing temperature without changing polymer composition, which was ascribed to the sliding motion of CB7 molecular containers around the donor DCH stalk in response to temperature changes (Figure 24).
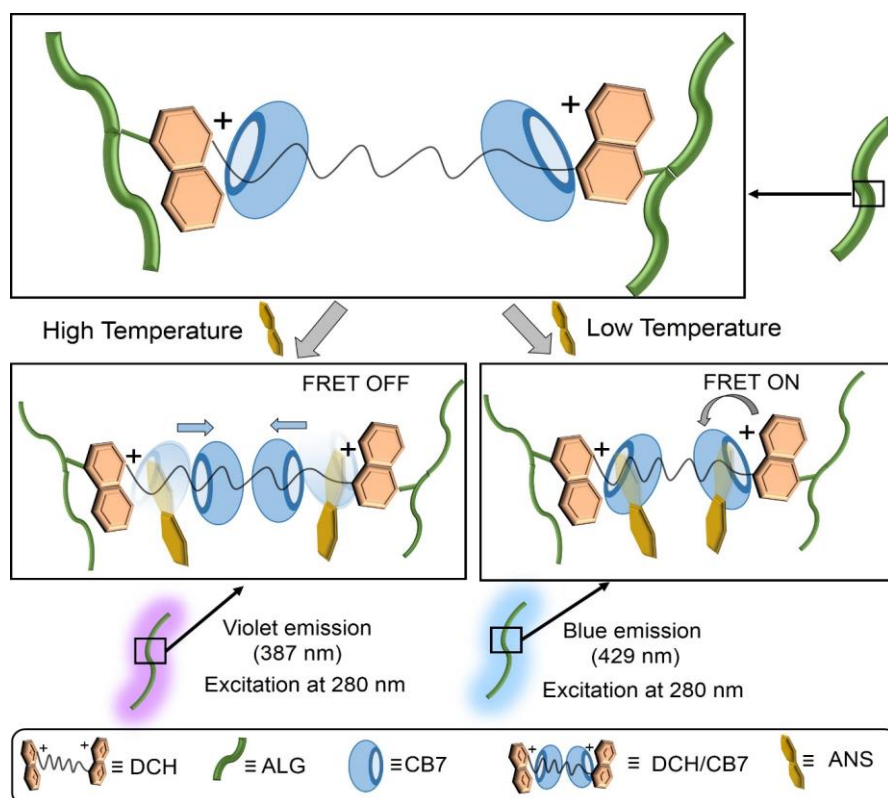

Figure 24: Illustration of the energy transfer process upon a temperature increase from 298 K (low temperature) to 368 K (high temperature). With increasing temperature, CB7 moves along the stalk away from the ANS toward the center, switching off the FRET signal.

Over the past years, the number of publications on FRET-based supramolecular architectures for harvesting light energy has substantially increased.[10−12,14,15,44−55] These publications describe derivatives of several parent fluorophores such as pyrene,[45] benzothiadiazole,[46] aminonaphthalene,[46,52] phenylenevinylene,[15,34] tetraphenylethene,[11,47,51] Nile Red,[12,34] stilbazolium,[48] porphyrin,[35,49] eosin Y,[12,47] salicylaldehyde azine,[12,36] rhodamines,[36] boron dipyrromethene,[11,35,48−50,53] diphenylanthracene,[55] and perylene[45] as donors and/or acceptors. The employed macrocycles include cucribituril,[14,15,47,52] cyclodextrin,[14,34,36,49] calixarenes,[46] pillararenes,[11,12,35,50,51,54,55] and heterorotaxane.[14] The emission color has been tuned in the range of violet to red for excitation in the UV (335−383)[11,12,14,34−36,45,55] and visible (470−490)[49,50] regions. In most cases, reversible responsiveness was modulated by chemical stimuli,[14,49] and the fabricated materials were applied in fluorescent inks,[15,46] optical switches,[15,47] biological probes,[11] solar cells,[45] organic-inorganic hybrid gels,[45] optoelectronics,[50] protein assembly,[11] enzymatic assays,[11] cancer cell diagnosis,[11] color tuning,[12,14,15] photosynthesis mimicking,[11,34,36] artificial light harvesting,[36, 48−50] and security encryption.[14] However, compared to all previously reported artificial light-harvesting systems, the distinct feature of the materials prepared herein is their responsiveness to temperature based on the shuttling of CB7 along the DCH stalk (Figure 16), which obviates the need to change the ratio of donor and acceptor components.[14,46] Moreover, our supramolecular architecture can be simply fabricated by one-step formation of amide linkages between the amino groups of DCH and the carboxylic groups of ALG. Finally, the new supramolecular polymers are non-toxic and biologically active, and could therefore find biomedical applications in the future.[16,17]

Chapter 4: Conclusion

This study describes the synthesis of a bioactive supramolecular carbohydrate polymer by grafting of cucurbit[7]uril macrocycle (CB7)-encapsulated dequalinium chloride hydrate (DCH) onto alginic acid carbohydrates and shows that light energy transfer based on energy migration can be controlled by changing polymer temperature but not polymer composition. Our study makes a significant contribution to literature, as CB7 shuttling along the DCH stalk results in responsiveness to temperature and obviates the need to change the ratio of donor and acceptor components, which makes our system superior to previously reported ones and paves the way to the fabrication of further tunable-emission polymers for diverse applications. Further, we believe that the developed supramolecular polymers are non-toxic and biologically active and could therefore find numerous biomedical applications in the future.

References

1. Huang, P.; Gao, Y.; Lin, J.; Hu, H.; Liao, H.; Yan, X.; Tang, Y.; Jin, A.; Song, J.; Niu, G. Tumor-Specific Formation of Enzyme-Instructed Supramolecular Self-Assemblies as Cancer Theranostics. *ACS Nano.* 2015, *9*, 9517-9527.

2. Gust, D. Supramolecular Photochemistry Applied to Artificial Photosynthesis and Molecular Logic Devices. *Faraday Discuss.* 2015, *185*, 9-35.

3. Wu, H.; Chen, Y.; Liu, Y. Reversibly Photoswitchable Supramolecular Assembly and its Application as a Photoerasable Fluorescent Ink. *Adv. Mat.* 2016, *29*, 1605271.

4. Xiao, T.; Zhong, W.; Zhou, L.; Xu, L.; Sun, X.; Elmes, R.; Hu, X.; Wang, L. Artificial Light-Harvesting Systems Fabricated by Supramolecular Host–Guest Interactions. *Chin Chel Lett.* 2019, *30*, 31-36.

5. Hole, B.; Cowan, R.; Sawatzky, G.; Fink, J.; Fuggle, J. New Probe for the Ground-State Electronic Structure of Narrow-Band and Impurity Systems. *Phys. Rev. B.* 1985, *31*, 6856-6858.

6. Al-Dmour, H.; Alzard, R.; Alblooshi, H.; Alhosani, K.; AlMadhoob, S.; Saleh, N. Enhanced Energy Conversion of Z907-Based Solar Cells by Cucurbit[7]Uril Macrocycles. *Front Chem.* 2019, *7*, 561.

7. Malm, A.; Corbett, J. Improved Dynamic Light Scattering Using an Adaptive and Statistically Driven Time Resolved Treatment of Correlation Data. *Sci. Rep.* 2019, *9,* 13519.

8. Ferraris, S.; Cazzola, M.; Peretti, V.; Stella, B.; Spriano, S. Zeta Potential Measurements on Solid Surfaces for in Vitro Biomaterials Testing: Surface Charge, Reactivity upon Contact with Fluids and Protein Absorption. *Front Bioeng Biotech.* 2018, *6*, 60.

9. Shah, F.; Ruscsák, K.; Palmquist, A. 50 Years of Scanning Electron Microscopy of Bone a Comprehensive Overview of the Important Discoveries Made and Insights Gained into Bone Material Properties in Health, Disease, and Taphonomy. *Bone. Res.* 2019, 7, 15.

10. Lou, X.; Song, N.; Yang, Y. Fluorescence Resonance Energy Transfer Systems in Supramolecular Macrocyclic Chemistry. *Molecules* 2017, *22*, 1640.

11. Teunissen, A.; Pérez-Medina, C.; Meijerink, A.; Mulder, W. Investigating Supramolecular Systems Using Förster Resonance Energy Transfer. *Chem. Soc. Rev.* 2018, *47*, 7027−7044.

12. Xiao, T.; Zhong, W.; Zhou, L.; Xu, L.; Sun, X.; Elmes, R.; Hu, X.; Wang, L. Artificial Light-Harvesting Systems Fabricated by Supramolecular Host−Guest Interactions. *Chin. Chem. Lett.* 2019, *30*, 31–36.

13. Mako, T. L.; Racicot, J. M.; Levine, M. Supramolecular Luminescent Sensors. *Chem. Rev.* 2019, *119*, 322−477

14. Hou, X.; Ke, C.; Bruns, C.; McGonigal, P.; Pettman, R.; Stoddart, J. Tunable Solid-State Fluorescent Materials for Supramolecular Encryption. *Nat. Commun.* 2015, *6*, 6884.

15. Ni, X.; Chen, S.; Yang, Y.; Tao, Z. Facile Cucurbit[8]uril-Based Supramolecular Approach to Fabricate Tunable Luminescent Materials in Aqueous Solution. *J. Am. Chem. Soc.* 2016, *138*, 6177−6183.

16. Lee, K.; Mooney, D. Alginate: Properties and Biomedical Applications. *Prog. Polym. Sci.* 2012, *37*, 106−126.

17. Mallick, S.; Song, S.; Bae, Y.; Choi, J. Self-Assembled Nanoparticles Composed of Glycol Chitosan-Dequalinium for Mitochondria-Targeted Drug Delivery. *Int. J. Biol. Macromol.* 2019, *132*, 451−460.

18. Kosower, E.; Kanety, H.; Dodiuk, H.; Striker, G.; Jovin, T.; Boni, H.; Huppert, D. Intramolecular Donor-Acceptor Systems. 7. Solvent Dielectric Relaxation Effects on the Photophysics of 6-(Phenylamino)-*N*,*N*-dimethyl-2-naphthalenesulfonamides. *J. Phys. Chem.* 1983, *14*, 2479−2484.

19. Liu, S. M.; Ruspic, C.; Mukhopadhyay, P.; Chakrabarti, S.; Zavalij, P. Y.; Isaacs, L. The Cucurbit[n]uril Family: Prime Components for Self-Sorting Systems. *J. Am. Chem. Soc.* 2005, *127*, 15959−15967.

20. Freeman, W. A.; Mock, W. L.; Shih, N. Y. Cucurbituril. *J. Am. Chem. Soc.* 1981, *103*, 7367−7368.

21. Tang, B.; Li, W.; Jiao, Y.; Lu, J.; Xu, J.; Wang, Z.; Li, J.; Zhang, X. A Supramolecular Radical Cation: Folding-Enhanced Electrostatic Effect for Promoting Radical-Mediated Oxidation. *Chem. Sci.* 2018, *9*, 5015−5020.

22. Gong, W.; Yang, X.; Zavalij, P.; Isaacs, L.; Zhao, Z.; Liu, S. From Packed "Sandwich" To "Russian Doll": Assembly by Charge-Transfer Interactions in Cucurbit[10]uril. *Chem. Eur. J.* 2016, *22*, 17612−17618.

23. Ko, Y. H.; Kim, H.; Kim, Y.; Kim, K. U-Shaped Conformation of Alkyl Chains Bound to a Synthetic Host. *Angew. Chem., Int. Ed.* 2008, *47*, 4106−4109.

24. Li, S.; Xu, X.; Zhou, Y.; Zhao, Q.; Liu, Y. Reversibly Tunable White-Light Emissions of Styrylpyridiniums with Cucurbiturils in Aqueous Solution. *Org. Lett.* 2017, *19*, 6650−6653.

25. Chernikova, E.; Tkachenko, S.; Fedorova, O.; Peregudov, A.; Godovikov, I.; Shepel, N.; Minkovska, S.; Kurutos, A.; Gadjev, N.; Deligeorgiev, T. G.; Fedorov, Y. V. Multistep Assembling *via* Intermolecular Interaction Between (Bis)Styryl Dye and Cucurbit[7]uril: Spectral Effects and Host Sliding Motion. *Dyes Pigm.* 2016, *131*, 206−214.

26. Baroncini, M.; Gao, C.; Carboni, V.; Credi, A.; Previtera, E.; Semeraro, M.; Venturi, M.; Silvi, S. Light Control of Stoichiometry and Motion in Pseudorotaxanes Comprising a Cucurbit[7]uril Wheel and an Azobenzene-Bipyridinium Axle. *Chem. Eur. J.* 2014, *20*, 10737−10744.

27. Chernikova, E.; Berdnikova, D.; Fedorov, Y.; Fedorova, O.; Maurel, F.; Jonusauskas, G. Light-Induced Piston Nanoengines: Ultrafast Shuttling of a Styryl Dye Inside Cucurbit[7]uril. *Phys. Chem. Chem. Phys.* 2017, *19*, 25834−25839.

28. Ling, X.; Samuel, E.; Patchell, D.; Masson, E. Cucurbituril Slippage: Translation is a Complex Motion. *Org. Lett.* 2010, *12*, 2730−2733.

29. Willis-Fox, N.; Belger, C.; Fennell, J.; Evans, R.; Swager, T. Threading the Needle: Fluorescent Poly-Pseudo-Rotaxanes for Size-Exclusion Sensing. *Chem. Mater.* 2016, *28*, 2685−2691.

30. Lee, J. W.; Samal, S.; Selvapalam, N.; Kim, H.-J.; Kim, K. Cucurbituril Homologues and Derivatives: New Opportunities in Supramolecular Chemistry. *Acc. Chem. Res.* 2003, *36*, 621−630.

31. Masson, E.; Ling, X.; Joseph, R.; Kyeremeh-Mensah, L.; Lu, X. Cucurbituril Chemistry: A Tale of Supramolecular Success. *RSC Adv*. 2012, *2*, 1213−1247.

32. Saleh, N.; Ghosh, I.; Nau, W. M. Cucurbiturils in Drug Delivery and for Biomedical Applications. In *Supramolecular Systems in Biomedical Fields*;

Schneider, H.-J., Ed.; Royal Society of Chemistry: Cambridge (UK), 2013; pp. 164−212.

33. Giri, R. Fluorescence Quenching of Coumarins by Halide Ions. *Spectrochim. Acta* 2004, *60*, 757−763.

34. Li, J.; Chen, Y.; Yu, J.; Cheng, N.; Liu, Y. A Supramolecular Artificial Light-Harvesting System with an Ultrahigh Antenna Effect. *Adv. Mater.* 2017, *29*, 1701905.

35. Wajahat, A.; Li, X.; Fang, L.; Gonsg, W.; Ning, G. Construction of New Cross-Linked Supramolecular Polymer with FRET Phenomenon Based on Oligo(P-Phenylenevinylene)-Linked Pillar[5]Arene Dimer. *Supramol. Chem.* 2017, *30*, 72−79.

36. Lian, Z.; Jiang, M.; Qiao, F.; Yuan, Z.; Chen, M.; Wang, R.; Zhang, T.; Xu, L.; Yan, H.; Zhuo, S. Xing, L. B. Significant Enhancement of Light-Harvesting Efficiency through the Formation of [2]Pseudorotaxane with γ-Cyclodextrin Based on a Bolaamphiphile of Salicylaldehyde Azine Moiety. *Dyes Pigm.* 2019, *162*, 475−480.

37. Dryza, V.; Bieske, E. Electron Injection and Energy-Transfer Properties of Spiropyran–Cyclodextrin Complexes Coated onto Metal Oxide Nanoparticles: Toward Photochromic Light Harvesting. *J. Phys. Chem. C* 2015, *119*, 14076−14084.

38. Guo, S.; Song, Y.; He, Y.; Hu, X.-Y.; Wang, L. Highly Efficient Artificial Light-Harvesting Systems Constructed in Aqueous Solution Based on Supramolecular Self-Assembly. *Angew. Chem., Int. Ed.* 2018, *57*, 3163−3167.

39. Wagner, B.; Stojanovic, N.; Day, A.; Blanch, R. Host Properties Of Cucurbit[7]uril: Fluorescence Enhancement of Anilinonaphthalene Sulfonates. *J. Phys. Chem. B* 2003, *107*, 10741−10746.

40. Valeur, B. Molecular Fluorescence: Principles and Applications. In *Molecular Fluorescence*; Wiley-VCH: New York, Heidelberg, 2002.

41. Seliskar, C.; Brand, L. Electronic Spectra of 2-Aminonaphthalene-6-Sulfonate and Related Molecules. II. Effects of Solvent Medium on the Absorption and Fluorescence Spectra. *J. Am. Chem. Soc.* 1971, *93*, 5414−5420.

42. Dey, S.; Sreenivasan, K. Conjugation of Curcumin onto Alginate Enhances Aqueous Solubility and Stability of Curcumin. *Carbohydr. Polym.* 2014, *99*, 499−507.

43. Sarika, P. R.; James, N. R.; Kumar, P. R.; Raj, D. K.; Kumary, T. V. Gum Arabic-Curcumin Conjugate Micelles with Enhanced Loading for Curcumin Delivery to Hepatocarcinoma Cells. *Carbohydr. Polym.* 2015, *134,* 167−174.

44. Peres, I.; Coelho, M. Encapsulation of Active Compounds: Particle Characterization, Loading Efficiency and Stability. Doctor of Philosophy in Chemical and Biological Engineering, University of Porto France, 2011.

45. Danaei, M.; Dehghankhold, M.; Ataei, S.; Hasanzadeh Davarani, F.; Javanmard, R.; Dokhani, A.; Khorasani, S.; Mozafari, M. Impact of Particle Size and Polydispersity Index on the Clinical Applications of Lipidic Nanocarrier Systems. *Pharmaceutics* 2018, *10*, 57, 10020057.

46. Chen, J.; Liu, Y.; Mao, D.; Ma, D. Acyclic Cucurbit[n]uril Conjugated Dextran for Drug Encapsulation and Bioimaging. *Chem. Commun.* 2017, *53*, 8739−8742.

47. Xu, Z.; Peng, S.; Wang, Y.; Zhang, J.; Lazar, A.; Guo, D. Broad-Spectrum Tunable Photoluminescent Nanomaterials Constructed from a Modular Light-Harvesting Platform Based on Macrocyclic Amphiphiles. *Adv. Mater.* 2016, *28*, 7666−7671.

48. Qiao, F.; Yuan, Z.; Lian, Z.; Yan, C.; Zhuo, S.; Zhou, Z.; Xing, L. Supramolecular Hyperbranched Polymers with Aggregation-Induced Emission Based on Host-Enhanced π–π Interaction for Use as Aqueous Light-Harvesting Systems. *Dyes Pigm.* 2017, *146*, 392−397.

49. Bojtár, M.; Szakács, Z.; Hessz, D.; Bazsó, F.; Kállay, M.; Kubinyi, M.; Bitter, I. Supramolecular FRET Modulation by Pseudorotaxane Formation of a Ditopic Stilbazolium Dye and Carboxylato-Pillar[5]Arene. *Dyes Pigm.* 2016, *133*, 415−423.

50. Gu, Z.; Guo, D.; Sun, M.; Liu, Y. Effective Enlargement of Fluorescence Resonance Energy Transfer of Poly-Porphyrin Mediated by β-Cyclodextrin Dimers. *J. Org. Chem*. 2010, *75*, 3600−3607.

51. Meng, L.; Li, D.; Xiong, S.; Hu, X.; Wang, L.; Li, G. FRET-Capable Supramolecular Polymers Based on a BODIPY-Bridged Pillar[5]Arene Dimer with BODIPY Guests for Mimicking the Light-Harvesting System of Natural Photosynthesis. *Chem. Commun.* 2015, *51*, 4643−4646.

52. Wang, Y.; Lv, M.; Song, N.; Liu, Z.; Wang, C.; Yang, Y. Dual-Stimuli-Responsive Fluorescent Supramolecular Polymer Based on a Diselenium-Bridged Pillar[5]Arene Dimer and an AIE-Active Tetraphenylethylene Guest. *Macromolecules* 2017, *50*, 5759−5766.

53. Kushwaha, S.; Maity, A.; Gangopadhyay, M.; Ravindranathan, S.; Rajamohanan, P.; Das, A. Cucurbit[7]uril Induced Formation of FRET-Enabled Unilamellar Lipid　Vesicles. *Langmuir* 2017, *33*, 10989–10999.

54. Wang, S.; Ye, J.; Han, Z.; Fan, Z.; Wang, C.; Mu, C.; Zhang, W.; He, W. Highly Efficient FRET from Aggregation-Induced Emission to BODIPY Emission Based on Host–Guest Interaction for Mimicking the Light-Harvesting System. *RSC Adv.* 2017, *7*, 36021−36025.

55. Sun, C.; Peng, H.; Niu, L.; Chen, Y.; Wu, L.; Tung, C.; Yang, Q. Artificial Light-Harvesting Supramolecular Polymeric Nanoparticles Formed by Pillar[5]Arene-Based Host–Guest Interaction. *Chem. Commun.* 2018, *54*, 1117−1120.

List of publications

1. Sohail, A.; Alnaqbi, M.; Saleh, N. Alginate/Cucurbit[7]Uril/Dequalinium-Based Supramolecular Carbohydrates: Modulation Of FRET Signals By Temperature Control. *Macromolecules* 2019, *52*, 9023-9031.

2. Alzard, R.; Bufaroosha, M.; Al-Shamsi, N.; Sohail, A.; Al-Dubaili, N.; Salem, A.; Abdou, I.; Saleh, N. Solubilization Of Pyridone-Based Fluorescent Tag By Complexation In Cucurbit[7]Uril. *ACS Omega* 2019, *4*, 953-960.
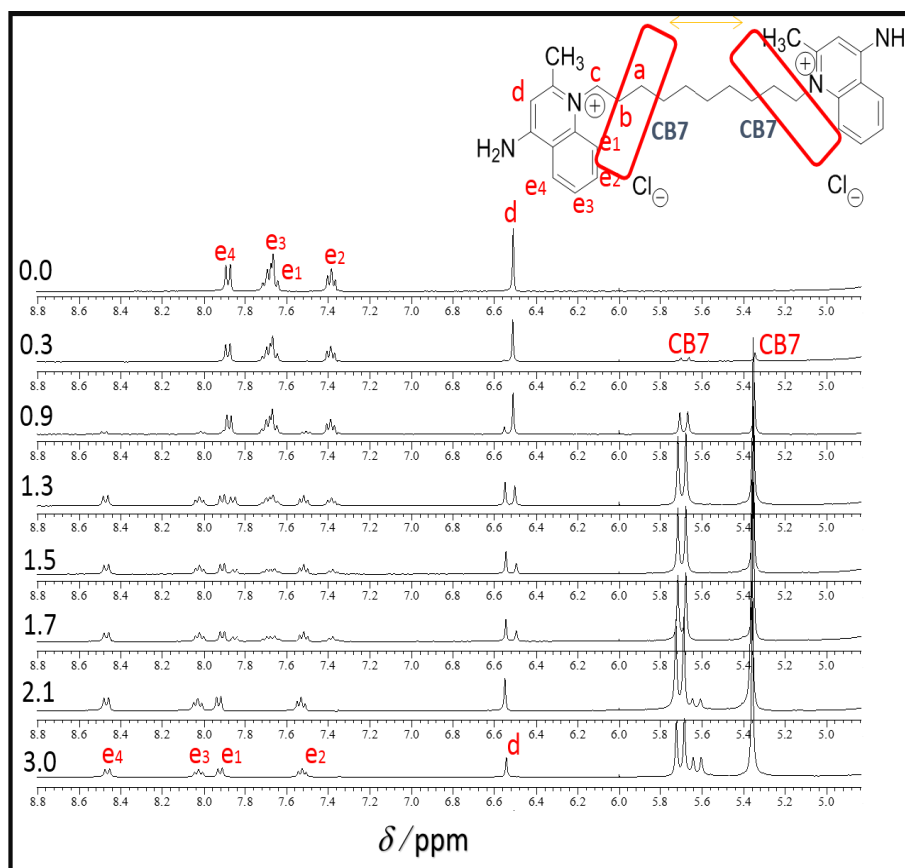
Appendix

Figure S1: ¹H NMR spectra of DCH (1.5 mM) with CB7 (0–3.0 equiv.) in D₂O with pD 7.0 (400 MHz).
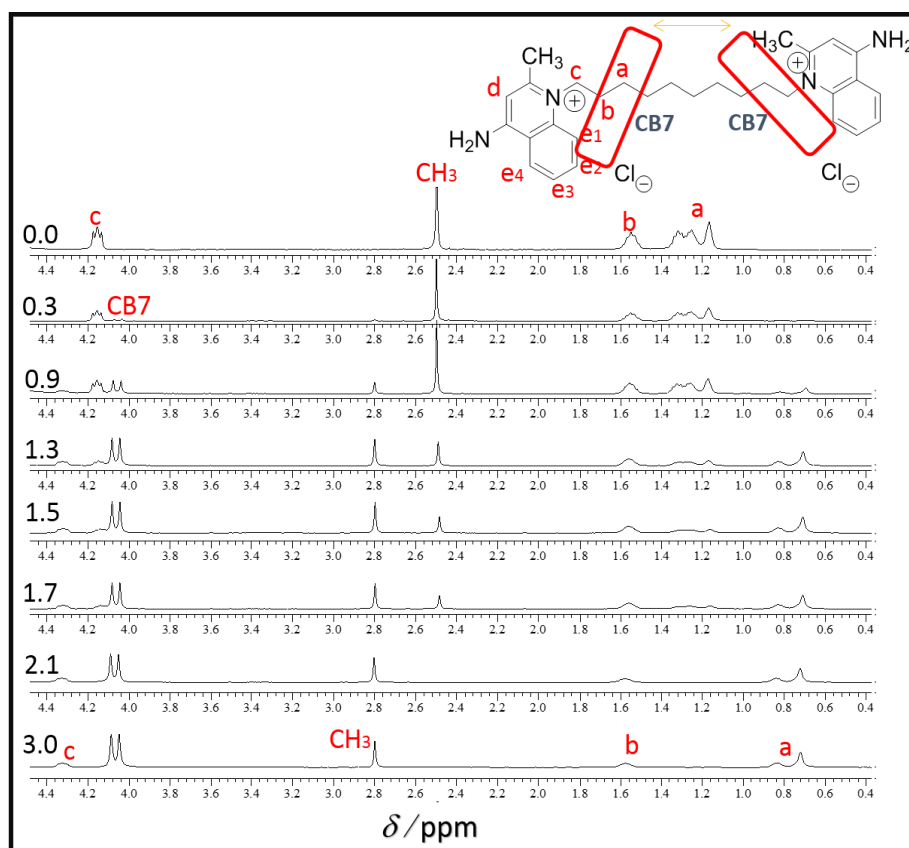
Figure S1: ^{1}H NMR spectra of DCH (1.5 mM) with CB7 (0–3.0 equiv.) in D$_2$O with pD 7.0 (400 MHz) (Continued).
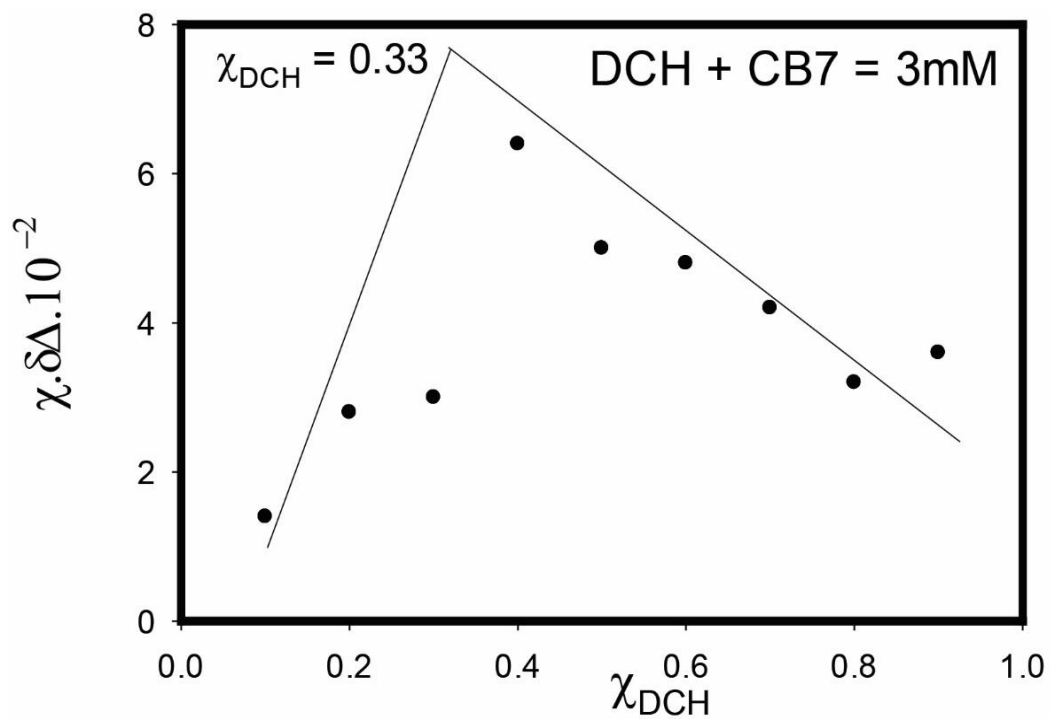
Figure S2: ^{1}H NMR spectra (400MHz, D_2O, pD 7.0, 298K). A job's plot for DCHCB7 the total concentration of guest DCH and host CB7 was fixed at 3 mM and the peak at 6.5 ppm in the bottom spectra was used in the calculation.
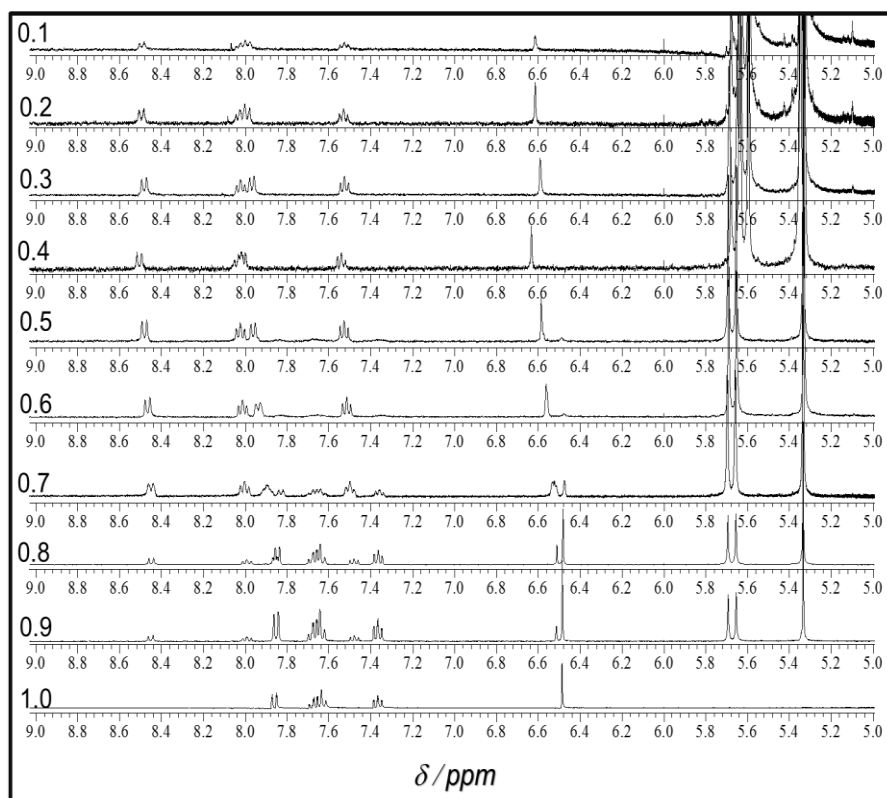
Figure S2: ^{1}H NMR spectra (400MHz, D$_2$O, pD 7.0, 298K). A job's plot for DCHCB7 the total concentration of guest DCH and host CB7 was fixed at 3 mM and the peak at 6.5 ppm in the bottom spectra was used in the calculation (Continued).
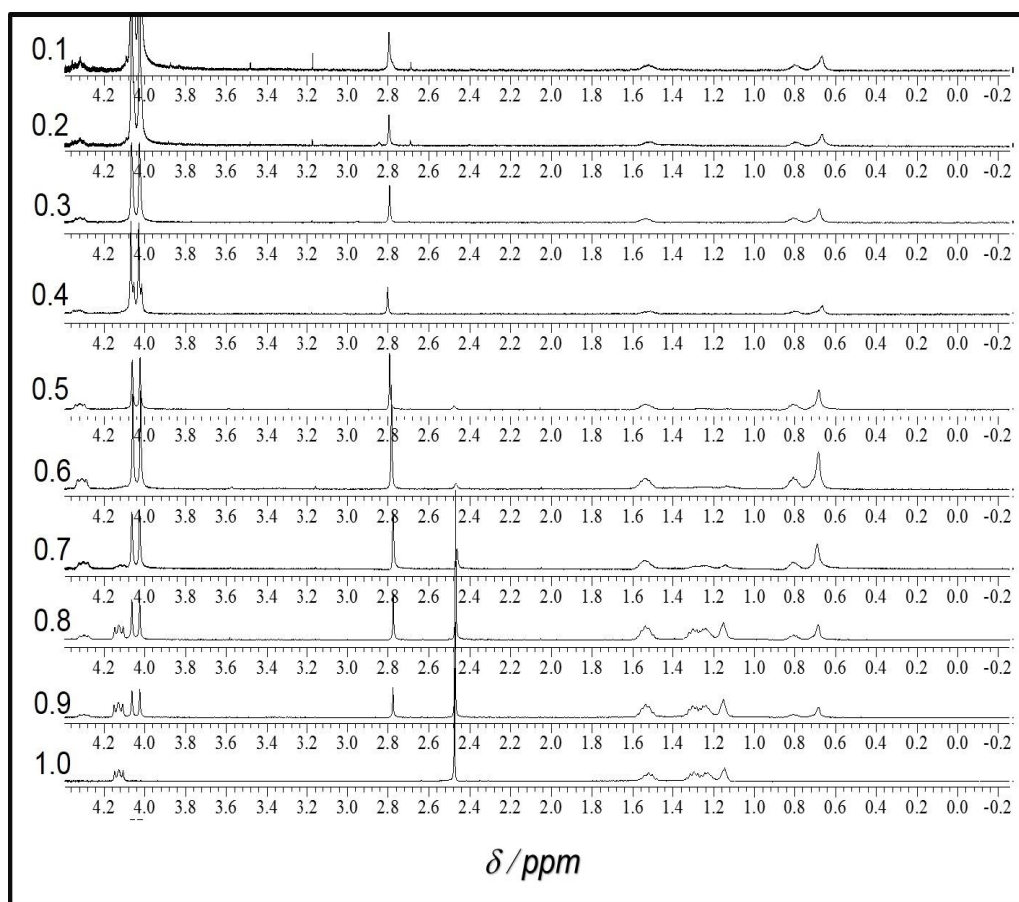
Figure S2: ^{1}H NMR spectra (400MHz, D$_2$O, pD 7.0, 298K). A job's plot for DCHCB7 the total concentration of guest DCH and host CB7 was fixed at 3 mM and the peak at 6.5 ppm in the bottom spectra was used in the calculation (Continued).
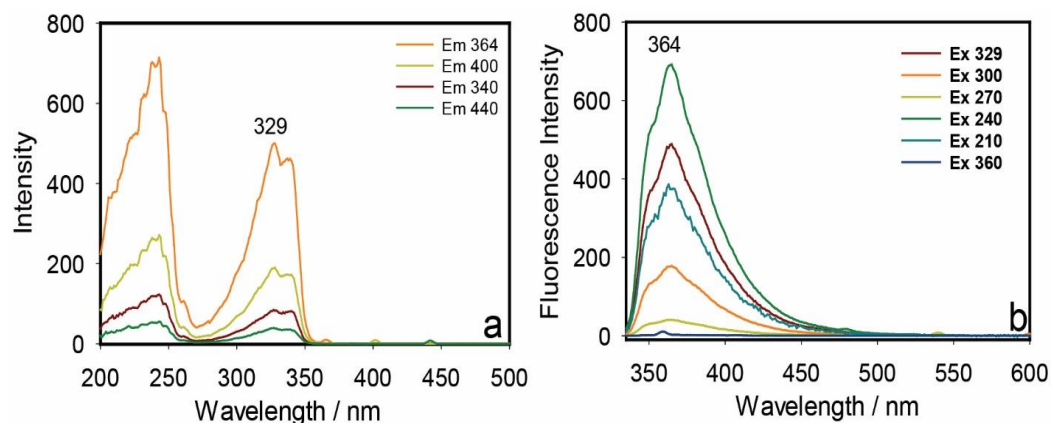
Figure S3: Excitation and excitation-dependence emission spectra of DCH (10 µM) at room temperature. The monitored emission and excitation wavelengths are shown in a and b, respectively.

Table S1: Excited-state lifetime constants along with the average lifetimes (see the Experimental Section) observed at 320 nm for DCHALG (1.5 mg/L, water suspension) at different concentrations of added ANS at 298 K. The calculated Förster radius (R_0) is also shown at each set of data points.

[ANS] / μM	τ_1/ ns	τ_2/ ns	τ_{avg}/ ns	R_o	χ^2
0	1.04	4.78	2.13		1.130
0.32	1.05	5.33	2.27	797.7	1.315
0.83	1.06	5.52	2.26	617.5	1.050
2.04	1.11	6.34	2.37	468.3	1.124
4.00	1.142	7.05	2.46	377.7	1.018
6.98	1.09	6.34	2.39	311.6	1.110
9.43	1.07	7.34	1.16	295.2	1.165
12.7	0.98	7.50	2.52	271.9	1.166
15.8	0.98	7.69	2.57	258.4	1.102
18.6	0.98	7.87	2.66	242.4	0.920
21.3	0.98	8.11	2.64	231.9	1.012
26.2	0.98	8.90	2.85	216.5	0.968
30.4	0.93	7.21	2.44	207.6	1.127
34.2	0.96	7.88	2.57	202.3	1.050

Time resolution was ~90 ps and the excitation wavelength was at 280 nm. Lifetime values are presented as mean ± standard deviation. The estimated experimental error was 2% for the lifetime around 1 ns and 20% for the lifetime around 2 ns. R_0 has an arbitrary unit as defined in FAST software (see Experimental Section).

Table S2: Excited-state lifetime constants along with the average lifetimes (see the Experimental Section) observed at 320 nm for DCH/CB7ALG (2.75 mg/L, water suspension) at different concentrations of added ANS at 298 K. The calculated Förster radius (R_0) is also shown at each set of data points.

[ANS] / μM	τ_1/ ns	τ_2/ ns	τ_3/ ns	τ/ ns	R_o	χ^2
0	1.11	3.58	7.58	4.43		1.021
0.08	0.28	1.93	6.11	4.16	1097.5	0.872
0.29	0.47	2.24	6.11	4.14	725.3	0.954
0.62	0.49	2.23	6.18	4.12	576.5	0.916
1.23	0.73	2.74	6.54	4.14	460.9	0.978
2.04	0.54	2.11	5.99	4.07	394.4	1.109
3.61	0.51	2.34	6.03	4.07	322.1	1.022
5.14	0.85	2.99	6.91	4.12	292.8	0.945
7.69	0.72	2.66	6.27	3.98	267.2	0.874
9.77	0.64	2.31	5.93	3.90	247.8	0.987
11.8	0.59	2.21	5.98	3.86	239.7	0.990
14.3	1.05	3.85	8.37	4.01	231.1	0.877
16.1	0.79	3.40	7.40	3.89	255.9	0.901
17.8	0.64	2.42	6.51	3.82	220.4	0.858
20.0	1.04	3.35	7.77	3.92	216.5	0.954
21.6	0.93	3.15	7.06	3.77	211.1	1.100
23.1	0.99	3.48	6.91	3.73	211.9	0.900
25.0	0.84	2.89	6.83	3.77	205.0	0.893
27.3	0.81	2.99	7.11	3.71	202.6	0.849
29.4	1.00	3.86	7.58	3.65	200.1	0.993
34.1	0.66	2.00	5.96	3.47	196.2	0.974

Time resolution was ~90 ps and the excitation wavelength was at 280 nm. Lifetime values are presented as mean ± standard deviation. The estimated experimental error was 2% for the lifetime around 1 ns and 20% for the lifetime around 2 ns. R_0 has an arbitrary unit as defined in FAST software (see Experimental Section).

Table S3: Excited-state lifetime constants along with the average lifetimes (see the Experimental Section) observed at 320 nm for DCH/CB7ALG (2.75 mg/L, water suspension) [ANS] = 0 μM at different temperatures.

Temp	τ_1/ ns	τ_2/ ns	τ_3/ ns	τ_{avg}/ ns	χ^2
25	1.48	5.49		4.03	1.08
45	0.69	2.23	5.29	3.61	1.09
65	0.32	1.74	4.11	2.93	0.87
95	0.79	2.79		2.19	0.74

Time resolution was ~90 ps and the excitation wavelength was at 280 nm. Lifetime values are presented as mean ± standard deviation. The estimated experimental error was 2% for the lifetime around 1 ns and 20% for the lifetime around 2 ns.

Table S4: Excited-state lifetime constants along with the average lifetimes (see the Experimental Section) observed at 320 nm for DCH/CB7ALG (2.75 mg/L, water suspension) [ANS] = 8.75 μM at different temperatures.

Temp	τ_1/ ns	τ_2/ ns	τ_3/ ns	τ_{avg}/ ns	χ^2
25	1.38	6.42		2.32	0.84
45	0.89	1.78	6.66	2.27	0.88
65	0.79	2.17	7.12	2.01	0.96
95	0.91	5.03		1.59	0.94

Time resolution was ~90 ps and the excitation wavelength was at 280 nm. Lifetime values are presented as mean ± standard deviation. The estimated experimental error was 2% for the lifetime around 1 ns and 20% for the lifetime around 2 ns.

Table S5: Excited-state lifetime constants along with the average lifetimes (see the Experimental Section) observed at 320 nm for DCH/CB7ALG (2.75 mg/L, water suspension) [ANS] = 14.3 μM at different temperatures.

Temp	τ_1/ ns	τ_2/ ns	τ_3/ ns	τ_{avg}/ ns	χ^2
25	1.26	6.98		2.41	0.95
45	0.78	1.96	7.59	2.30	0.84
65	0.74	1.44	5.44	1.91	1.89
95	0.80	4.39		1.58	0.90

Time resolution was ~90 ps and the excitation wavelength was at 280 nm. Lifetime values are presented as mean ± standard deviation. The estimated experimental error was 2% for the lifetime around 1 ns and 20% for the lifetime around 2 ns.

Table S6: Excited-state lifetime constants along with the average lifetimes (see the Experimental Section) observed at 320 nm for DCH/CB7ALG (2.75 mg/L, water suspension) [ANS] = 20.0 μM at different temperatures.

Temp	τ_1/ ns	τ_2/ ns	τ_3/ ns	τ_{avg}/ ns	χ^2
25	1.27	7.34		2.47	0.91
45	0.85	2.20	7.43	2.32	0.93
65	0.74	2.14	8.28	2.05	0.88
95	0.80	4.99		1.62	0.90

Time resolution was ~90 ps and the excitation wavelength was at 280 nm. Lifetime values are presented as mean ± standard deviation. The estimated experimental error was 2% for the lifetime around 1 ns and 20% for the lifetime around 2 ns.

Table S7: Excited-state lifetime constants along with the average lifetimes (see the Experimental Section) observed at 320 nm for DCH/CB7ALG (2.75 mg/L, water suspension) [ANS] = 27.3 μM at different temperatures.

Temp	τ_1/ ns	τ_2/ ns	τ_3/ ns	τ_{avg}/ ns	χ^2
25	1.15	6.89		2.46	0.89
45	0.85	2.19	9.19	2.50	0.87
65	0.79	2.77	9.89	2.31	0.92
95	0.86	5.37		1.73	0.96

Time resolution was ~90 ps and the excitation wavelength was at 280 nm. Lifetime values are presented as mean ± standard deviation. The estimated experimental error was 2% for the lifetime around 1 ns and 20% for the lifetime around 2 ns.

Table S8: Excited-state lifetime constants along with the average lifetimes (see the Experimental Section) observed at 320 nm for DCH/CB7ALG (2.75 mg/L, water suspension) [ANS] = 33.3 μM at different temperatures.

Temp	τ_1/ ns	τ_2/ ns	τ_3/ ns	τ_{avg}/ ns	χ^2
25	1.19	7.59		2.58	1.06
45	0.94	3.88	11.14	2.60	0.87
65	0.66	1.47	7.96	2.25	1.04
95	0.86	6.49		1.89	0.81

Time resolution was ~90 ps and the excitation wavelength was at 280 nm. Lifetime values are presented as mean ± standard deviation. The estimated experimental error was 2% for the lifetime around 1 ns and 20% for the lifetime around 2 ns.
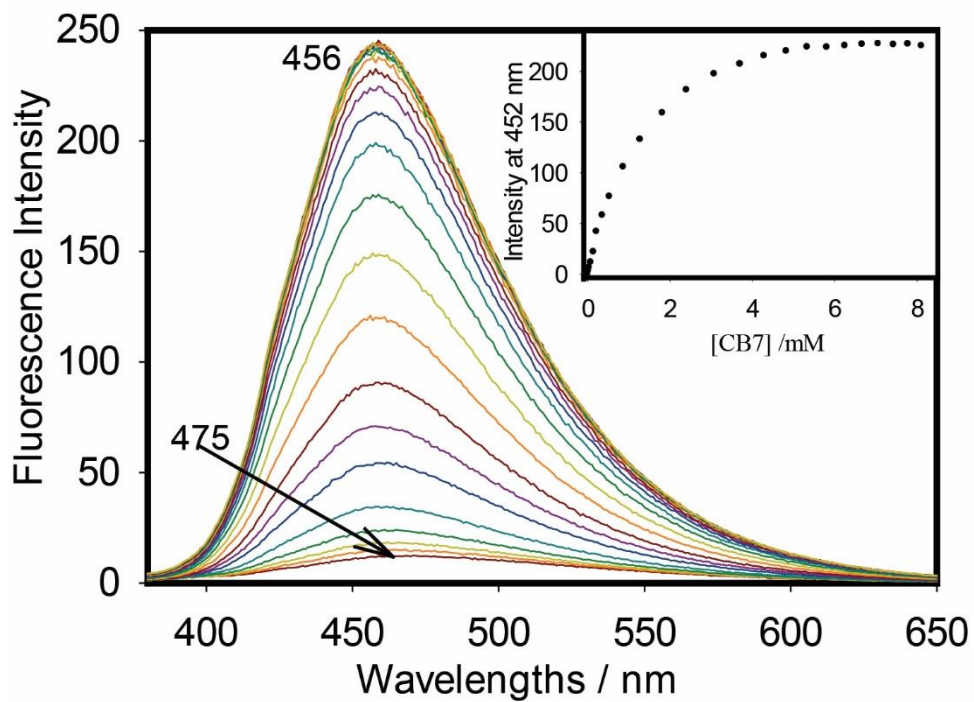
Figure S4: Fluorescence-binding titrations (excitation at 370 nm) of ANS (125 μM) with CB7 (up to 20 mM) at pH 7.3 in phosphate buffer at room temperature (Data were reproduced with permission from reference 46.
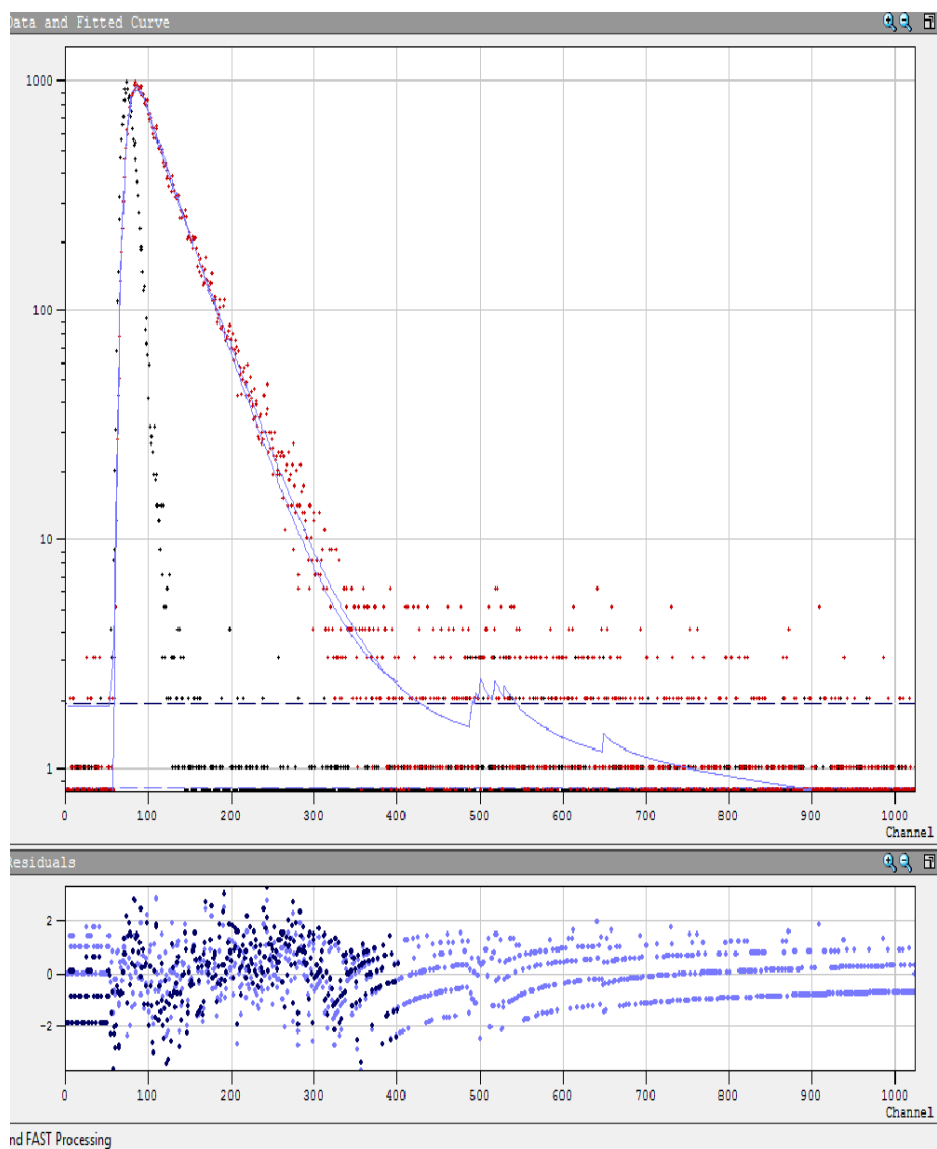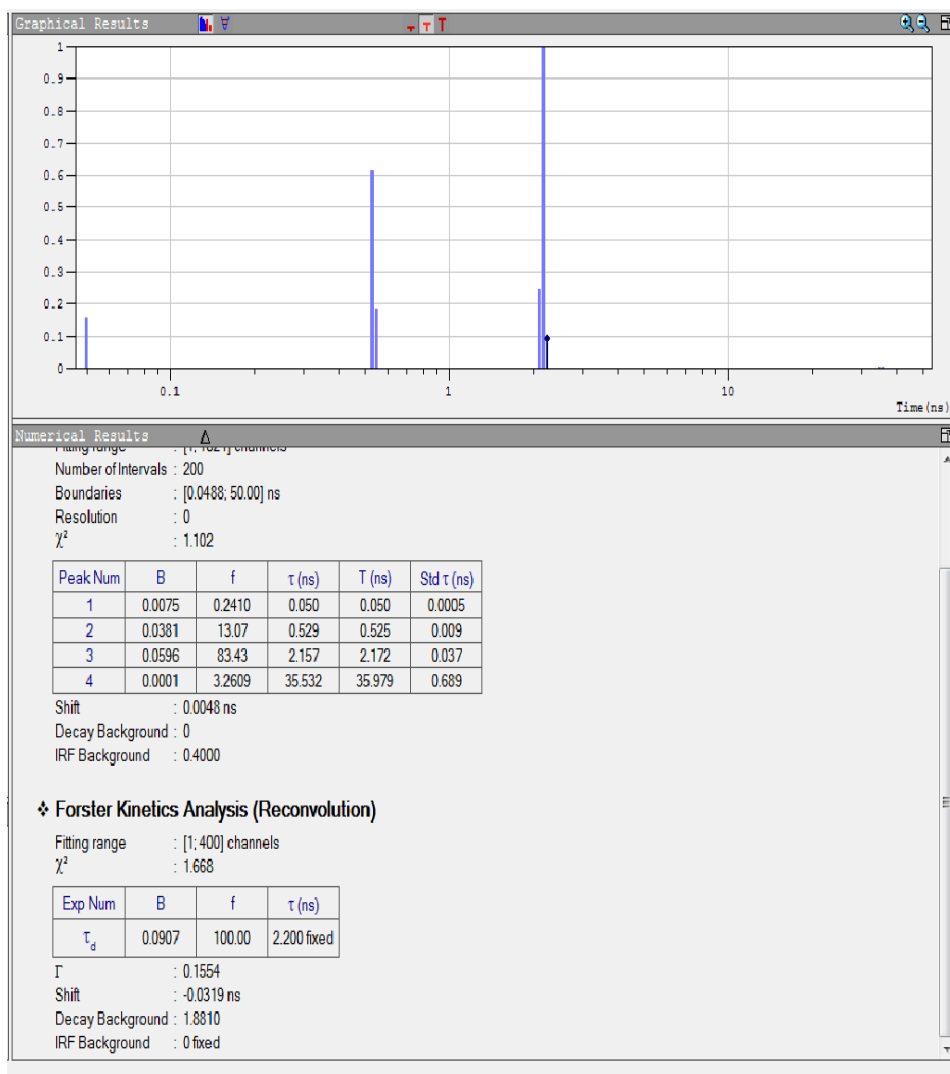
Figure S5: Förster Kinetic Analysis fit result for DCH/CB7 (10 µM + 5 equiv. CB7) with [ANS] = 14.3 µM at 298 K.

Figure S5: Förster Kinetic Analysis fit result for DCH/CB7 (10 µM + 5 equiv. CB7) with [ANS] = 14.3 µM at 298 K. (Continued)
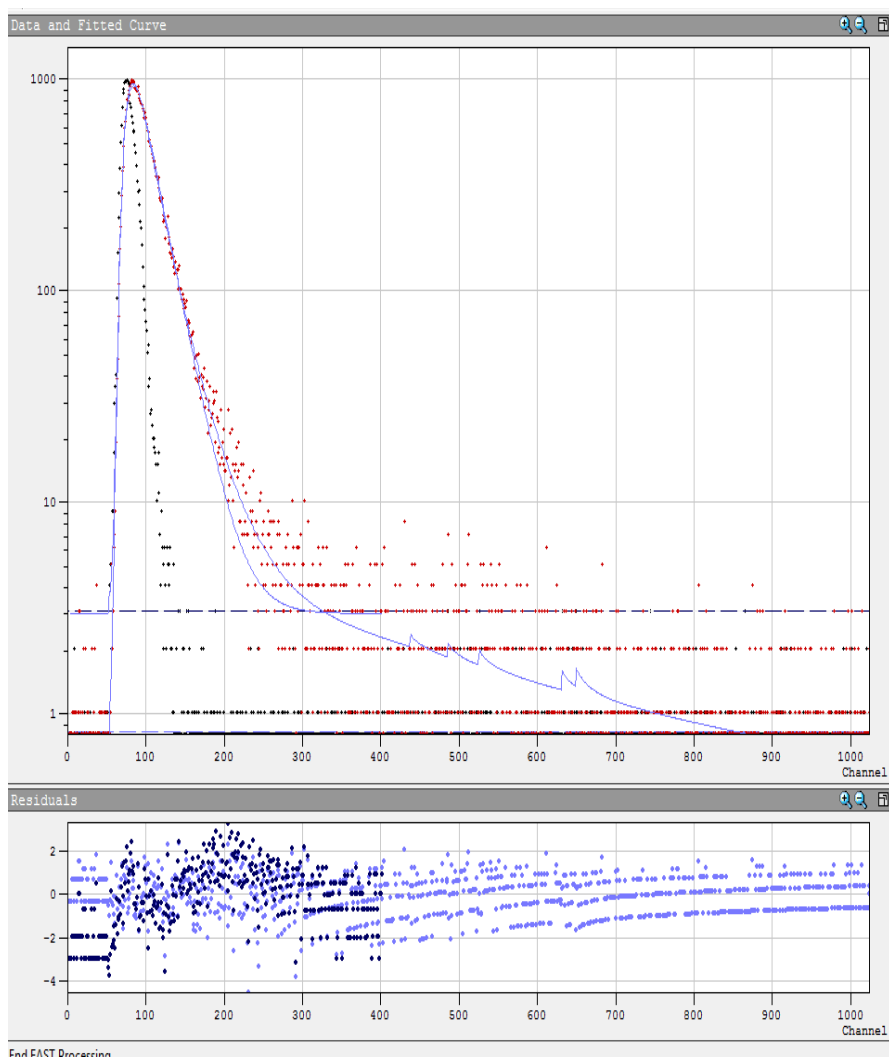
Figure S6: Förster Kinetic Analysis fit result for DCH (10 µM) with [ANS] = 7.69 µM at 298 K.
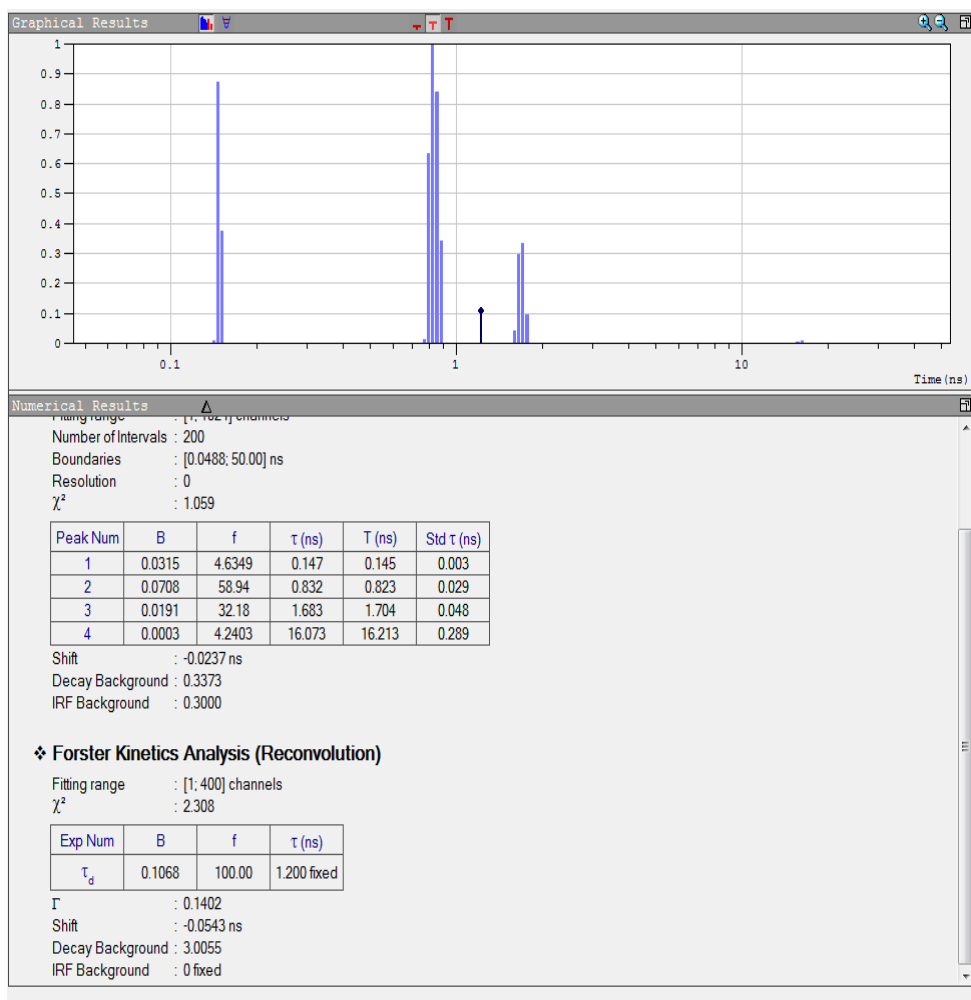
Figure S6: Förster Kinetic Analysis fit result for DCH (10 µM) with [ANS] = 7.69 µM at 298 K. (Continued)
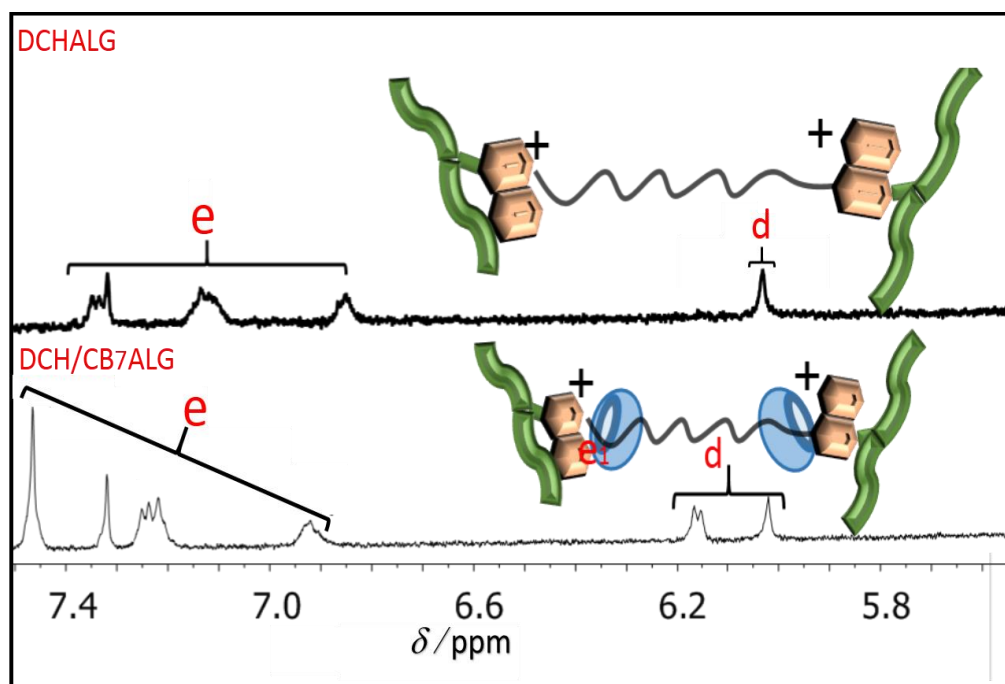
Figure S7: ^{1}H NMR spectra of DCHALG and DCH/CB7ALG (250 mg/mL) in D$_2$O/DMSO-d$_6$ (1:1) with pD ~7.0 (500 MHz) at 298 K.
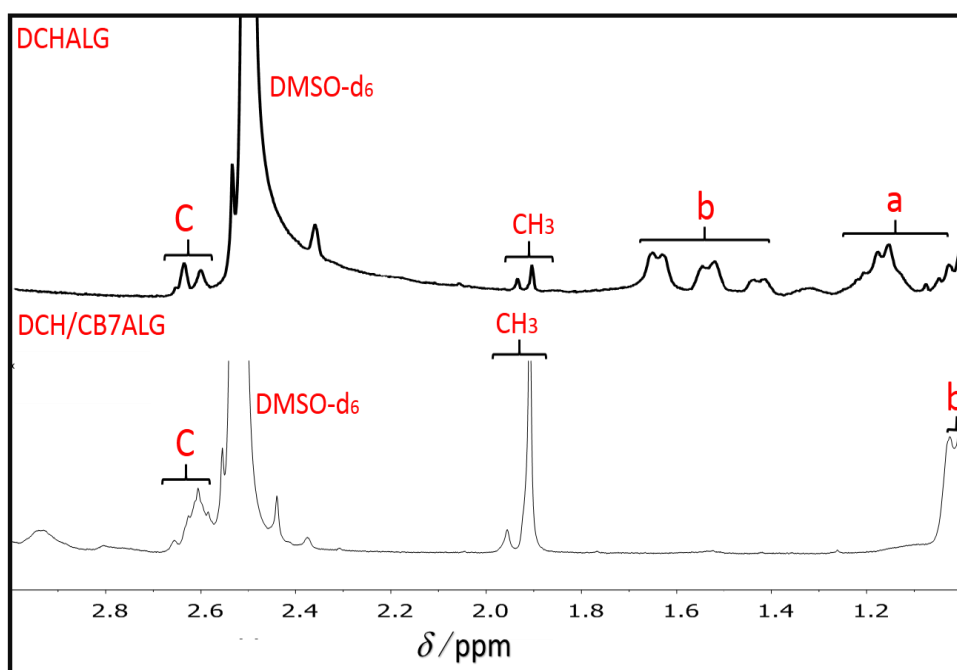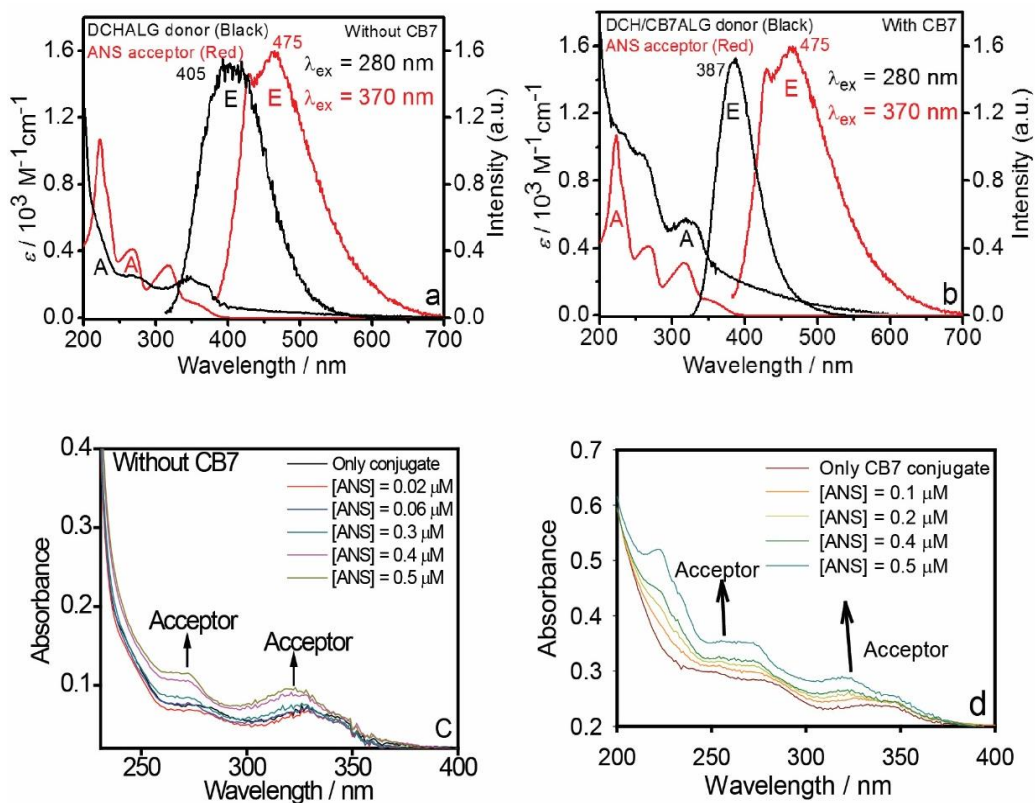

Figure S7: ^{1}H NMR spectra of DCHALG and DCH/CB7ALG (250 mg/mL) in D$_2$O/DMSO-d$_6$ (1:1) with pD ~7.0 (500 MHz) at 298 K. (continued)
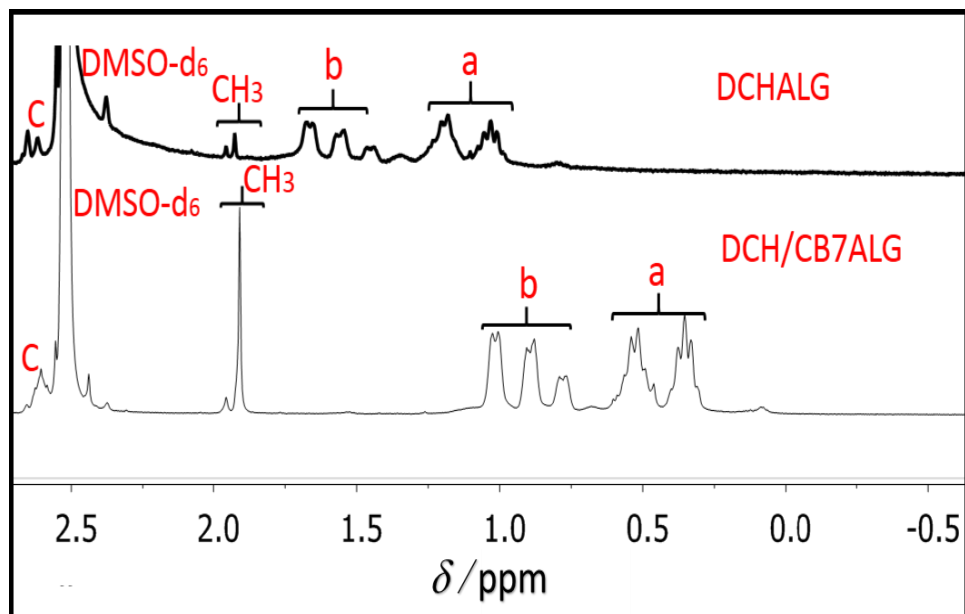
Figure S7: ^{1}H NMR spectra of DCHALG and DCH/CB7ALG (250 mg/mL) in D$_2$O/DMSO-d$_6$ (1:1) with pD ~7.0 (500 MHz) at 298 K. (continued)

Figure S8: Illustration of the spectral overlap between the donor DCHALG (black spectra) and the acceptor ANS (red spectra) in water suspension without (a) and with CB7 (b); The A and E labels are used for absorption and emission spectra, respectively. The UV−vis absorption spectral changes of DCHALG (1.5 mg/L, water suspension) upon the addition of different [ANS] concentrations without CB7 (c) and with 5 equiv. CB7 (d) as directly indicated in the plot.
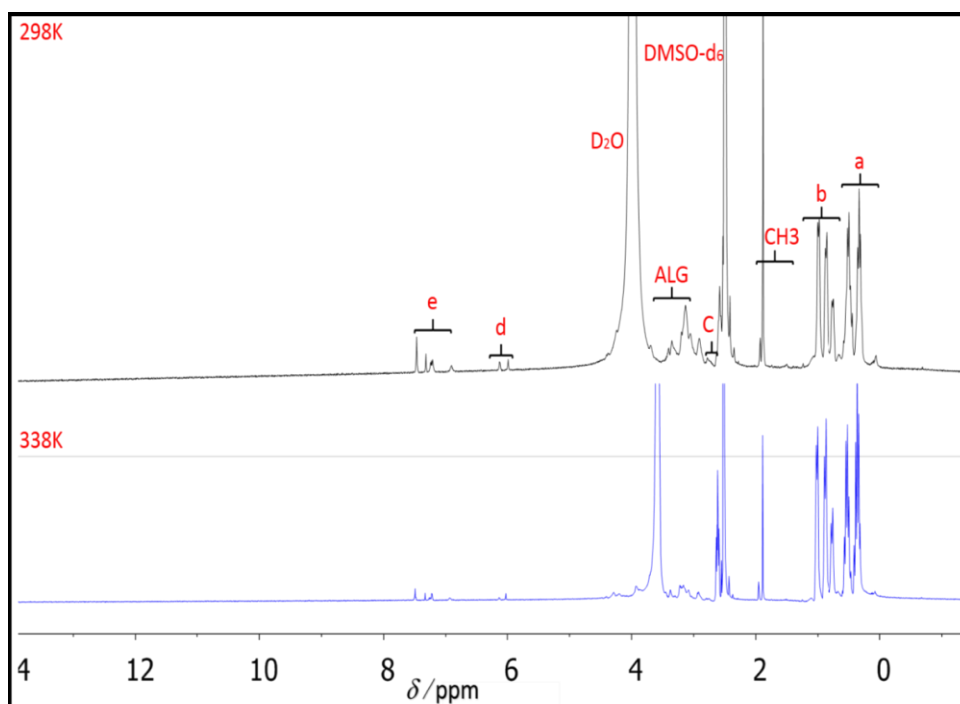
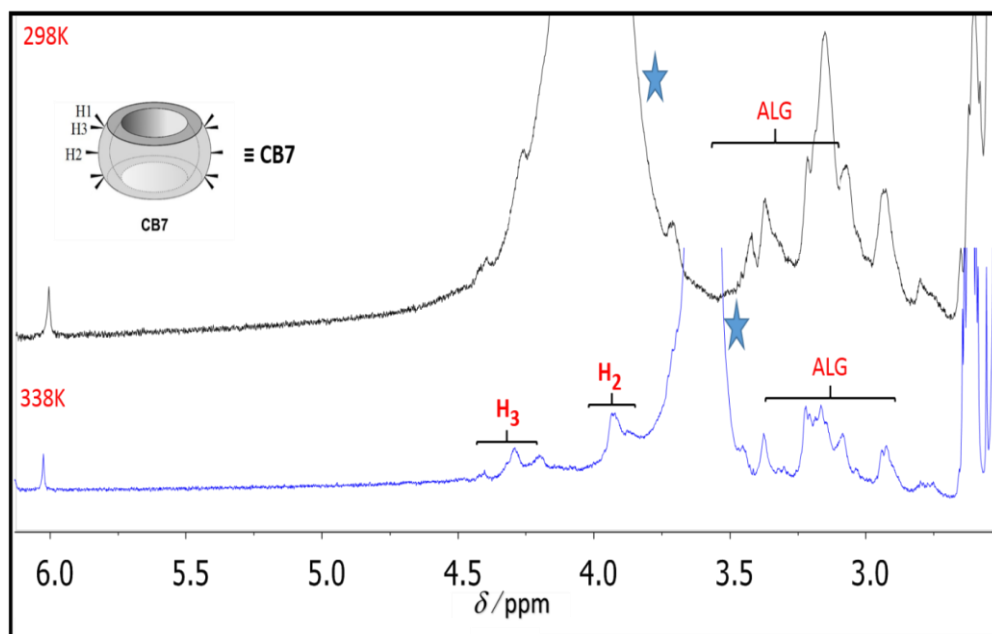Figure S9: ^{1}H NMR spectra of DCH/CB7ALG polymers (280 mg/mL) in D$_2$O/DMSO-d$_6$ (1:1) with pD ~7.0 (500 MHz).

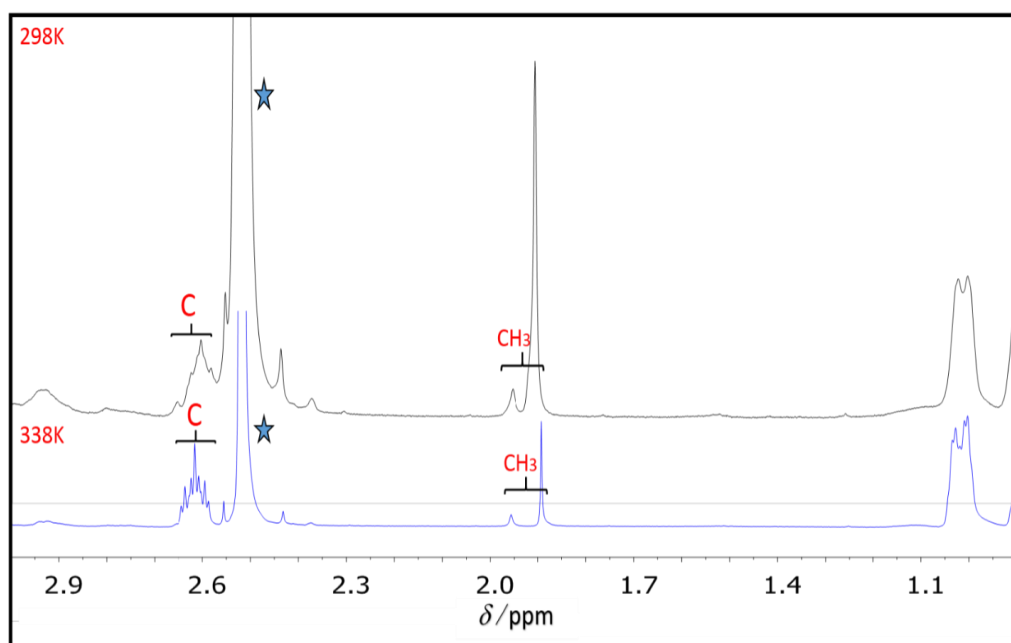Figure S9: ^{1}H NMR spectra of DCH/CB7ALG polymers (280 mg/mL) in D$_2$O/DMSO-d$_6$ (1:1) with pD ~7.0 (500 MHz) (Continued).

Figure S9: ^{1}H NMR spectra of DCH/CB7ALG polymers (280 mg/mL) in D$_2$O/DMSO-d$_6$ (1:1) with pD ~7.0 (500 MHz) (Continued).

Figure S9: ^{1}H NMR spectra of DCH/CB7ALG polymers (280 mg/mL) in D$_2$O/DMSO-d$_6$ (1:1) with pD ~7.0 (500 MHz) (Continued).

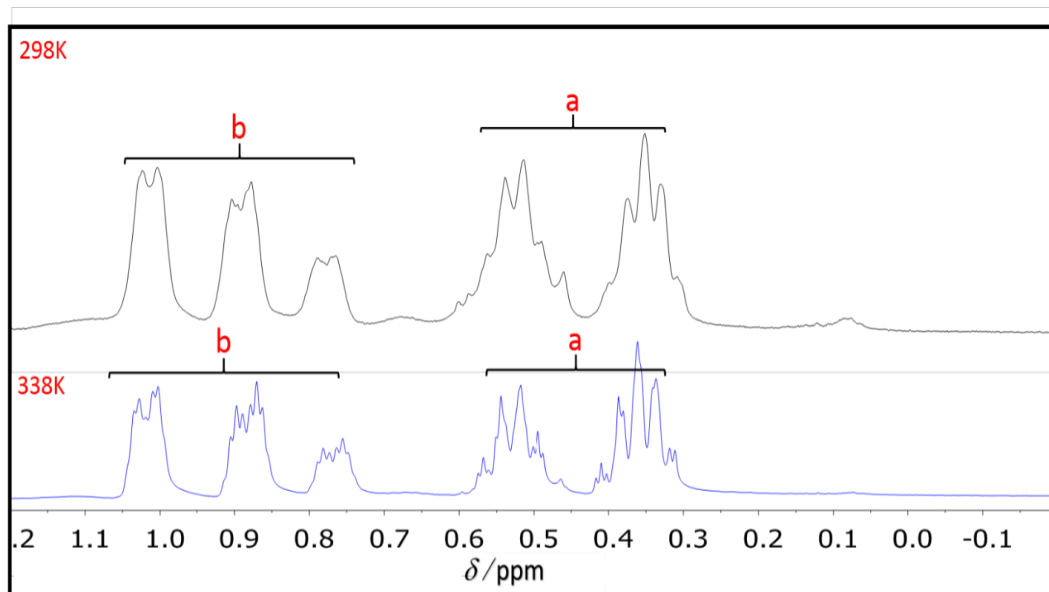Figure S9: ^{1}H NMR spectra of DCH/CB7ALG polymers (280 mg/mL) in D$_2$O/DMSO-d$_6$ (1:1) with pD ~7.0 (500 MHz) (Continued).